Mon. Not. R. Astron. Soc. **327,** 435–451 (2001)

A first detailed study of the colliding wind WR+O binary WR 30a

E. Gosset,★† P. Royer, G. Rauw,‡§ J. Manfroid¶ and J.-M. Vreux
Institut d'Astrophysique et de Géophysique, Université de Liège, Avenue de Cointe, 5, B-4000 Liège, Belgium

Accepted 2001 June 6. Received 2001 June 5; in original form 2001 February 12

ABSTRACT

We present a detailed, extensive investigation of the photometric and spectroscopic behaviour of WR 30a. This star is definitely a binary system with a period around 4.6 d. We propose the value $P = 4.619$ d ($\sigma = 0.002$ d). The identification of the components as WO4+O5((f)) indicates a massive evolved binary system; the O5 component is a main-sequence or, more likely, a giant star. The radial velocities of the O star yield a circular orbit with an amplitude $K_{\rm O} = 29.9$ ($\sigma = 2.1$) km s^{-1} and a mass function of 0.013 ($\sigma = 0.003$) $M_{\odot}$. The spectrum of WR 30a exhibits strong profile variations of the broad emission lines that are phase-locked with the orbital period. We report the detection of the orbital motion of the WO component with $K_{\rm WO} = 189$ km s^{-1}, but this should be confirmed by further observations. If correct, it implies a mass ratio $M_{\rm WO}/M_{\rm O} = 0.16$. The star exhibits sinusoidal light variations of amplitude 0.024 mag peak-to-peak with the minimum of light occurring slightly after the conjunction with the O star in front. On the basis of the phase-locked profile variations of the C IV λ4658 blend in the spectrum of the WO, we conclude that a wind–wind collision phenomenon is present in the system. We discuss some possibilities for the geometry of the interaction region.

Key words: binaries: spectroscopic – stars: individual: WR 30a – stars: mass-loss – stars: Wolf–Rayet.

1 INTRODUCTION

WR 30a was first suspected as a possible Wolf–Rayet (WR) star by McConnell & Sanduleak (1970) during a deep objective-prism survey performed around the Carina nebula region and was reported under the fourth entry of their catalogue (MS4) as an object of magnitude 14. Stenholm (1975), in his own survey, failed to detect it and MS4 was withdrawn from the list of WR stars. Fortunately, MS4 came back as a last minute entry in the sixth catalogue of galactic WR stars (van der Hucht et al. 1981) under the name of WR 29a: a spectrum taken by Conti was suggestive of a WR + abs classification, confirming the detection by McConnell & Sanduleak. Later, Lundström & Stenholm (1984b) published a spectrum of the star clearly exhibiting the emission lines of a WC4 star (domination of C IV $\lambda\lambda$5802–12, presence of C IV λ4658, weakness or actually absence of C III λ5696, O V λ5592 being weakly present) but no clear trace of absorption lines was visible. Nevertheless, the authors preserved the information from Conti and suggested a WC4 + abs classification. Independently, Moffat & Seggewiss (1984) confirmed the WC4 classification but noticed a dilution effect of the emission lines that they attributed to the presence of a hot O-type companion. They suggested a spectral type O4 ($\pm$ one subclass) for the absorption spectrum on the basis of the presence of He II λ4542 and λ5411, and of the apparent absence of He I λ4471. Lundström & Stenholm (1984a) remarked on the fact that MS4 should have appeared in the sixth catalogue under the name WR 30a instead of WR 29a. They also reported a magnitude $v = 13.7$ and a colour index $b - v = 0.58$ in the particular narrow band system of Smith (1968). From their spectroscopy, Smith, Shara & Moffat (1990a,b) derived somewhat different values: $v = 13.33$ and $b - v = 0.79$. They further reclassified WR 30a as WO4 + O4, motivated by the presence of O VI $\lambda\lambda$3811–34 (although relatively weak compared to the same line in the spectra of other WO stars) and by the relative strength and broadness of C IV $\lambda\lambda$5802–12. Kingsburgh, Barlow & Storey (1995) pointed out that the excitation of WR 30a, as measured by the ratio of O VI $\lambda\lambda$3811–34 to O V λ5592, is lower than that of usual WO4 stars. However, these authors support the use of the total absence of C III λ5696 as an additional criterion for a WO classification: WR 30a is thus clearly not a WC4. They therefore introduced a WO5 class for the WR component of WR 30a. They

★E-mail: gosset@astro.ulg.ac.be
†Chercheur Qualifié au FNRS.
‡Chargé de Recherches au FNRS.
§Visiting Astronomer, CTIO, National Optical Astronomy Observatories (NOAO). NOAO is operated by the Association of Universities for Research in Astronomy, Inc. under contract with the National Science Foundation.
¶Directeur de Recherches au FNRS.

confirmed the O4 (± one subclass) classification of the absorption-line component in good agreement with the conclusions of Moffat & Seggewiss (1984). Recently, Crowther, De Marco & Barlow (1998) presented a new quantitative classification for WC and WO stars and attributed to WR 30a a spectral type WO4 + O4. It should however be cautioned that the existence of the WO classification in general is still a matter of debate (see e.g. Norci et al. 1998; Polcaro et al. 1999). Crowther et al. (1998) suggested that the transition from WC to WO could reflect an increase in the ionization rather than further chemical enrichment.

Niemela (1995) reported the first radial velocity study for WR 30a. She noticed large variations of C IV λ4658 from night to night, suggesting that WR 30a might be a short period binary. She further reported on the existence of a Balmer progression in the radial velocities of the O4 absorption spectrum suggesting a strong stellar wind. A plot of the C IV emission-line velocity versus the He II absorption velocity clearly indicates that the two lines are exhibiting opposite binary motions: the apparent ratio of the velocities implying a low mass ratio $M_{\rm WO4}/M_{\rm O4} = 0.15$, although the radial velocity range explored by the C IV line could be overestimated because of line-profile variations.

In the present paper, we report on our photometric and spectroscopic investigation of this system. A preliminary outcome is available in Gosset et al. (1999). From our data, we presently derive a first value for the period of the system as well as constraints on the orbital motion of the binary. Our data further suggest that a colliding wind phenomenon is present in the system and we make a first attempt to study the geometry of the interaction region.

In Section 2, we present the observations on which our study is based. Section 3 deals with the determination of the period, whereas Section 4 investigates the spectrum of WR 30a and its different variations. Section 5 further discusses the nature of WR 30a and of the interaction between both components. The main conclusions are underlined in Section 6.

2 OBSERVATIONS

2.1 Photometry

Between 1997 March 16 and April 19 we performed differential photometry of WR 30a with the Bochum 0.6-m telescope at La Silla, Chile. The Cassegrain focus of the telescope was equipped with a direct camera and a Thomson 7882 charge-coupled device (CCD) detector (384 × 576 pixels) subtending a full field of 3.2 by 4.8 arcmin. All the observations have been performed through a Johnson *V* filter. The field of WR 30a is sufficiently populated so that we can use other stars on the same CCD frame as the comparison stars necessary for the differential measurements. The typical exposure time was fixed to 5 min. Some 105 independent frames have been acquired distributed all over the run. Flat-field calibrations were obtained daily on the dome, with occasional checks on the twilight sky. Because of rapid contamination of the CCD window environment by dust, it was necessary to compute specific flat-fields for every night. The high-frequency component of the spatial variations of sensitivity was estimated from the flats obtained before and after the night. It was found that the low-frequency component of the flats (dome and sky) was not satisfactory as it led to errors of up to 0.05 mag. A polynomial illumination correction, based on the photometry of field stars, was used to produce the final calibrations for each night. This was particularly important since the stars did not always appear at the same location on the CCD, because of the poor centring of the telescope and the premature absence of a guiding camera. All reductions were carried out with the National Optical Astronomy Observatories (NOAO) IRAF package and DAOPHOT (Stetson 1987) as well as with personal software.

On each reduced frame, we performed aperture photometry of all the objects down to some threshold. Only nine stars are systematically present and measurable on all the frames. These are WR 30a itself and anonymous stars labelled A–H, as shown in Fig. 1. We computed the differential magnitude time series for all the pair combinations of the eight stars in order to check which ones could be utilized as comparison stars. The best comparison stars turned out to be A, B and E. The dispersion in the differential magnitudes (e.g. A–B, B–E or A–E) is characterized by $\sigma = 0.007$ mag (corresponding to a precision on one measurement of $\sigma = 0.005$ mag). One could, in addition, use D, F, G and H, although D and G could be slightly problematic. The dispersion of the differential magnitudes is characterized by $\sigma = 0.008$ mag for F or H and $\sigma = 0.009$ mag for D or G. Star C turned out to be strongly variable (~0.1 mag peak-to-peak) exhibiting over the run a predominantly deterministic light curve with two different light minima. This star has of course been rejected from further processing of the present data. To our knowledge, this is the first report of its variability.

The simultaneous use of several comparison stars has the advantage of further reducing the random noise. Two attitudes were possible: either to use a small number of fully reliable comparison stars, or to utilize a larger number of stars whose photometric measurements would most likely be less good on average. We therefore decided to define several time series. The first one (S1) is formed from the differential magnitudes with respect to the mean of the three comparison stars A, B and E, i.e.

$$WR - \frac{A + B + E}{3}. \quad (1)$$

A second time series (S2) contains the differential magnitudes with respect to the composite comparison star (A, B, E, D, F, G, H), i.e.

$$WR - \frac{A + B + E + D + F + G + H}{7}. \quad (2)$$

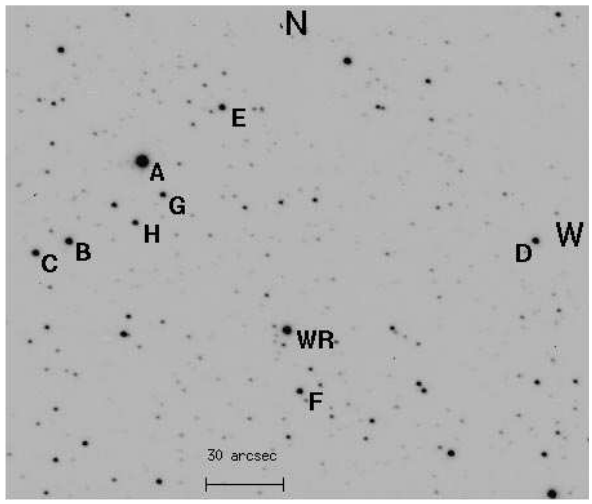

Figure 1. Finding chart for the field of WR 30a (WR). The stars labelled A–H are the comparison stars used for the photometry except star C that turned out to be strongly variable.

Both the S1 and S2 time series contain 105 measurements; S2 is expected to be slightly less noisy. Finally, we defined a third time series (S3) made of S2 from which we have rejected all the frames for which a truly discrepant value existed in at least one of the pair differential magnitudes of any combination of the seven comparison stars. This latter time series contains 80 measurements only, but represents the most accurate subset of the data. In Fig. 2, we present the light curve of WR 30a corresponding to the S1 time series. It is immediately clear that the WR star is photometrically variable: it is possible to count 6.5 cycles over a span of 30 d. This roughly corresponds to a 4.6-d period; the latter will be further discussed in Section 3.

On a few nights, we also observed standard stars in order to perform absolute photometry. We deduced for WR 30a a value $V = 12.73$ ($\sigma = 0.03$) mag. This result is in good agreement with the work of Wramdemark (1976): indeed, star 18 in his field BBII is actually WR 30a, and it is characterized by $V = 12.75$ mag ($B - V = 1.04$ mag and $U - B = -0.22$ mag).

2.2 Spectroscopy

An explorative spectrum of WR 30a in the blue–violet range (3800–4770 Å) was acquired on the night of 1996 April 8–9 with the European Southern Observatory (ESO) 1.5-m telescope equipped with the Boller and Chivens Cassegrain spectrograph. Further medium-resolution spectra in approximately the same wavelength range were obtained during two observing runs in 1996 May (seven nights, one spectrum per night, ~3800–4750 Å) and 1997 March (six nights, two spectra per night, ~3850–4800 Å) with the same instrument. In all these runs, we used the holographic grating (ESO # 32) with 2400 lines per mm, providing a reciprocal dispersion of 32.6 Å mm^{-1}. The detector was the new thinned, UV flooded CCD (ESO # 39). It is a Loral 2048 by 2048 array of 15-μm pixels. The gain was set to 1.2 e$^-$/ADU and the readout noise amounted to 7 e$^-$ rms. Helium–argon spectra were acquired with the telescope pointing to WR 30a just before or after the science exposure in order to minimize the effects of the spectrograph flexure. Dome flats were acquired at the beginning and end of the nights at several exposure levels in order to be able to search for possible non-linearities. The slit width was set to 215–220μm corresponding to 2 arcsec on the sky. The resulting spectral resolution element as measured on the helium–argon calibration spectra is 1.2 Å. The typical exposure time on WR 30a was 30 min.

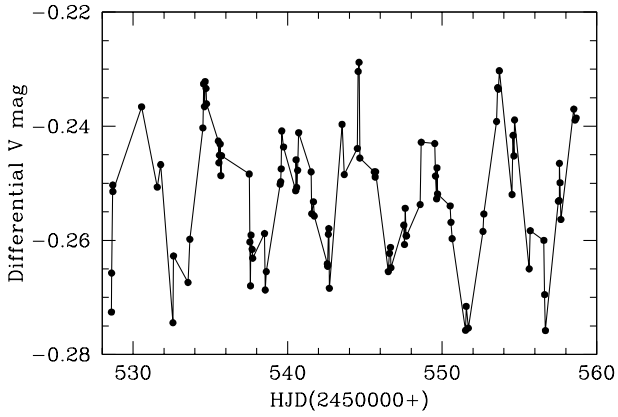

Figure 2. Plot of the differential V mag (time series S1) of WR 30a as a function of the HJD. The variability is evident; 6.5 cycles can be counted over the whole run. The continuous lines are given in order to guide the eyes but have no reality (interpolation is meaningless).

Part of the data are more or less strongly affected by a strange fringing effect (Turatto, Tighe & Castillo 1997) that contaminates the wavelength range 4050–4250 Å in the present instrument configuration. This fringing pattern is strongly variable and thus is usually different on the science exposure and on the flat-fields. In order to avoid amplification and increase of the intricacy of the phenomenon in the final stellar spectra, we decided that the data should not be flat-fielded.

All the reductions were performed using a local version of the MIDAS software developed at ESO.

End of 1999 May, a further five night run took place at the Cerro Tololo Interamerican Observatory (CTIO, Chile) 1.5-m telescope equipped with the Ritchey-Chrétien (Cassegrain) spectrograph. Unfortunately, awfully bad weather conditions prevailed and only one spectrum of WR 30a could be acquired, on the night of 1999 May 24–25. A 1-h exposure time was needed. The spectrograph was equipped with grating # 47 used in the second order with a Schott BG38 filter. The domain covered extended from 4277 to 4925 Å. The detector was a Loral 1200 × 800 CCD array of 15-μm pixels. The slit width, fixed to 110.5 μm, corresponded to 2 arcsec on the sky. The spectral resolution element as deduced

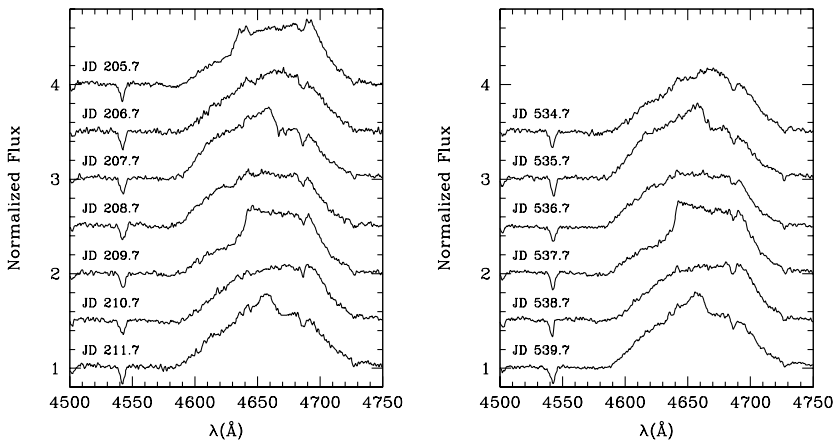

Figure 3. The line-profile variations of the C IV λ4658 line in WR 30a as observed in the spectra of our 1996 (left panel) and 1997 (right panel) runs. The spectra are normalized to the continuum and a shift of 0.5 continuum unit corresponds to 1 d. The HJD in the format HJD–245 0000 is used to label the spectra. The spectrum on HJD 245 0534.7 is quasi-identical to the one acquired on HJD 245 0206.7 and this remarkable likeness is preserved for each of the following pairs of spectra.

from the width of the helium–argon lines of the comparison spectra is about 1.5 Å.

All the extracted spectra have been normalized to the continuum and smoothed with a running boxcar of 1.2 Å. The individual spectra from the 1996 May run are displayed in Fig. 3 (left panel) for the part around the C IV λ4658 line. Clear line-profile variations are present from one night to the next, but the sequence does not seem to be ruled by any logic. In Fig. 3 (right panel), we plot the equivalent of the left panel for the 1997 run. The two spectra acquired each night were averaged for these 1997 data. It is immediately noticeable that the first spectrum of 1997 at HJD 245 0534.7 (HJD ≡ Heliocentric Julian Date) is extremely similar to the second one of the 1996 run at HJD 245 0206.7. This is also true for the five subsequent pairs of spectra. The emission-line profiles appear to exhibit fully deterministic variations unveiling a structure of the wind that remains stable on a time-scale of 1 yr.

To study the nature of WR 30a better, we built up mean spectra for each year by first cleaning the individual spectra for any strongly deviating pixel and then by computing the median of the 1996 data and the median of the 1997 data. Both mean spectra are very similar. A composite spectrum made by merging both mean spectra has been created and is shown in Fig. 4. It should be mentioned that the line profile of C IV λ4658 in this composite spectrum has of course no physical meaning, being a mean over different unevenly distributed phases. Apart from this line, another emission line related to the WR component is visible on the blue side of the spectrum: it is the doublet O VI λλ3811–34. The absorption spectrum related to the O companion is also clearly visible.

3 DETERMINATION OF THE PERIOD

3.1 From the photometry

We submitted the photometry of WR 30a to a detailed Fourier analysis in order to search for the period. We used the method of Heck, Manfroid & Mersch (1985, hereafter HMM, see Appendix A) which has the advantage of being a better expression for the power spectrum than for example the one of Scargle (1982). A daily regularity is enshrined in the time pattern of observations and all the three data sets (S1, S2, S3) exhibit a strong 1-d aliasing in their spectral windows (those of S1 and S2 are of course identical). The amplitude spectrum of the S3 time series is given in Fig. 5. As for the other two series, the amplitude spectrum is dominated by a family of aliases with peaks at $\nu = 0.21$, 0.79, $1.21\,\mathrm{d}^{-1}$ and so on. The dominating member of the family is always the one at $\nu = 0.21\,\mathrm{d}^{-1}$; the exact position of the peak being, respectively for S1, S2 and S3, at $\nu = 0.2127$, 0.2129 and $0.2143\,\mathrm{d}^{-1}$, corresponding to periods ranging from 4.66 to 4.70 d. The natural width of the Fourier peaks is $0.033\,\mathrm{d}^{-1}$, which translates into a value of 0.65 d on the period. Even if we admit an error of one tenth of the natural width on the peak position, the period could still be anywhere between 4.60 and 4.77 d. As can be seen from Fig. 5, the family of aliases is clearly outstanding; the frequency is highly significant.

The Fourier technique of HMM is, at each individual frequency, equivalent to a least-squares fitting of a cosine to the data. Only one frequency is treated at a time. As a generalized approach, we extended the method of HMM to perform a simultaneous fitting of

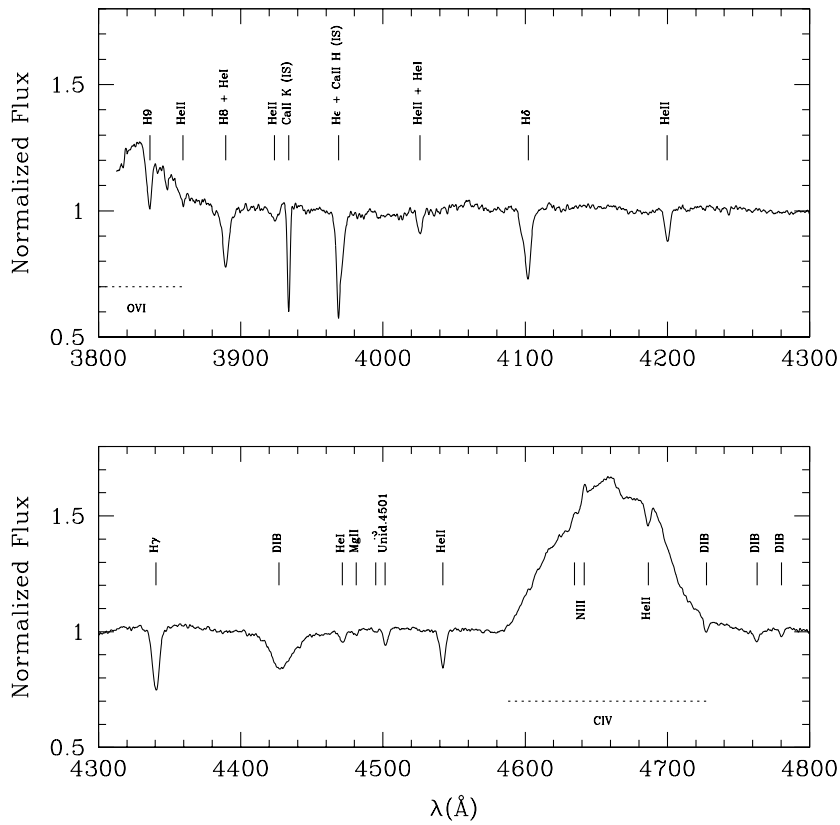

Figure 4. Composite spectrum of WR 30a generated from our observations of 1996 and 1997. The absorption spectrum of the O star is clearly visible. The lines are designated by vertical tick marks with labels; the detailed identification can be found in Table 2. The ticks labelled with N III correspond to narrow emission lines. DIB stands for diffuse interstellar band. The horizontal dashed lines indicate the broad emission lines of the WO component. The shape of the C IV line has no physical meaning since it corresponds to a mean over different unevenly distributed phases.

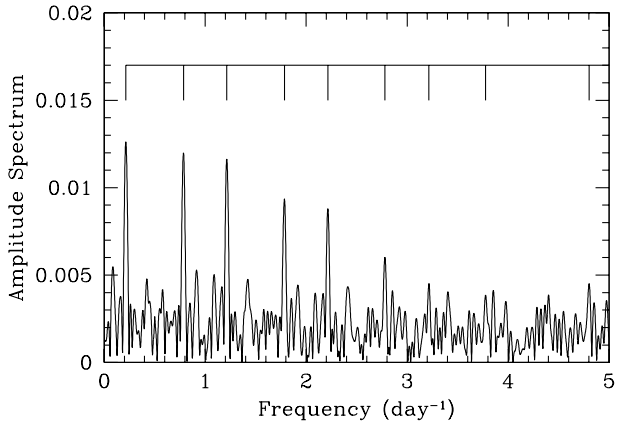

Figure 5. Amplitude spectrum of the time series (S3) of the differential V mag. The abscissae give the frequency expressed in d^{-1}. One family of 1-d aliases (pseudo-Nyquist frequency $0.5\,d^{-1}$) is outstanding, the highest peak of which is at $\nu = 0.214\,d^{-1}$. Tick marks indicate the members of the family. Another regularity linked to the nightly sampling induces a second pseudo-Nyquist frequency around $\nu = 8\,d^{-1}$. We computed the amplitude spectrum beyond the part shown here up to $\nu = 20\,d^{-1}$; neither a higher peak nor another family were detected.

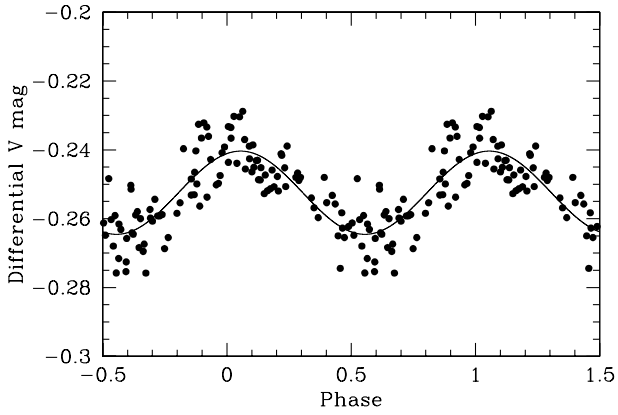

Figure 6. Phase diagram ($P = 4.619$ d, see Section 3.2) of the differential V mag (time series S1). The light curve is essentially sinusoidal as underlined by the fitted sine curve of semi-amplitude 0.012 mag. WR 30a presents a minimum of light at phase $\phi = 0.053$. Phase zero is defined at $T_0 =$ HJD 245 0535.095 and corresponds to the conjunction with the O star in front (see Section 4.1.2).

several frequencies (some kind of higher order Fourier) taking into account the correlations existing among the Fourier values at different frequencies as a result of the uneven sampling. This can easily be done by extending the HMM matrix $\boldsymbol{A}(\nu)$ ($N_{\rm obs}$ by 2) to a $N_{\rm obs}$ by $2M$ matrix where M is the number of frequencies to adjust simultaneously (see Appendix A). If we iterate on the number of frequencies, we obtain a method similar to the one described by Foster (1995). We iteratively performed a series of M frequency fittings where M ranged from 1 to 4. At each stage, the power spectrum was pre-whitened for the $M-1$ frequencies already detected and the classical power spectrum of the residuals (pre-whitened data) was computed using the HMM method and the highest peak searched for. The frequency relevant to this highest peak was then added to the $M-1$ frequencies already detected, and an M frequency fitting using the extended method was performed in order to adjust simultaneously the values of the M frequencies. The secondary and higher order frequencies found in the photometry in this way never turned out to be significant in any of the time series and always corresponded to amplitudes below $\sigma = 0.005$ mag (i.e. below the noise level). In addition, the set of secondary frequencies was different from one time series to the other. This clearly indicates that we are reaching the noise level. As a conclusion, only one frequency is well present in the photometric data set. The value of this detected frequency is robust with respect to the different sets of secondary frequencies.

We also applied Renson's method (1978) to analyse the three time series and we found that the lowest values of the relevant statistics were located at $\nu = 0.215\,d^{-1}$ for S1 and S2, and at $\nu = 0.216\,d^{-1}$ for S3, in good agreement with the Fourier analysis. Each of these values were standing in a dip having the natural width. The centroids of these dips were usually situated at a smaller frequency by some 0.003–0.004 d^{-1}.

As a result of these different analyses, we decided to adopt the value of $\nu = 0.214\,d^{-1}$ for the frequency derived from the photometry. The amplitude associated to this frequency is 0.024 mag (peak-to-peak, as deduced from the power spectrum, $\sigma =$ 0.002 mag) and $T_{\rm min} =$ HJD 245 0535.34 ($\sigma = 0.01$) corresponds to a minimum of light (as deduced from the phase of the Fourier transform). The variations are sinusoidal as can be seen in Fig. 6.

3.2 From the spectroscopy

Since the profile variations of the C IV λ4658 line look periodic (see Fig. 3), we deduced that the spectroscopic data could also be used to derive a value for the period. To this aim, we decided to characterize the line profile by its first-order moment W_1 defined by the following formula:

$$W_1 = \left(\frac{c}{\lambda_0 v_\infty}\right)^2 \int_{\lambda_1}^{\lambda_2} (F_\lambda - 1)(\lambda - \lambda_0)\,{\rm d}\lambda, \qquad (3)$$

where F_λ is the flux in the line normalized to the continuum (in a heliocentric reference frame). The integration runs from $\lambda_1 =$ 4580 to $\lambda_2 = 4730$ Å and the central wavelength is taken to be $\lambda_0 = 4658$ Å; c is the speed of light and v_∞ is the terminal velocity of the wind assumed to be equal here to 4500 km s^{-1} as given by Kingsburgh et al. (1995). The first-order moment has been measured on all the individual spectra and the resulting values are given in Table 1 along with the corresponding HJD.

We applied the Fourier technique of HMM and the method of Renson (1978) to the time series of W_1 as given in Table 1. Both methods are in remarkably good agreement; a family of 1-yr aliases is predominantly detected in the range 0.21–0.22 d^{-1}, in good concordance with the $\nu = 0.214\,d^{-1}$ value obtained from the photometry. Fig. 7 exhibits the run of Renson's statistic as a function of the frequency in the domain of interest. The regularity of the alias members is easily noticed. The longer span of time covered by the spectroscopy induces a much narrower natural width than for the photometry (potentially allowing a better precision), but the important gaps with no data imply a strong aliasing. The deepest dip is at $\nu = 0.2165\,d^{-1}$ whereas the second one is at $\nu = 0.2227\,d^{-1}$. The third and fourth ones are at $\nu =$ 0.2104 and 0.2256 d^{-1}. Other aliases exist at $\nu = 0.2074$, 0.2137 and 0.2193 d^{-1} but they are less important. The deepest dip at $\nu = 0.2165\,d^{-1}$ is certainly the best candidate from the analysis of the spectroscopic data alone. It is also the second closest alias to the value derived from the photometry. The first one at $\nu =$ 0.2137 d^{-1} is not amongst the deepest dips. It is very unfortunate that only one spectrum could be acquired during the CTIO run:

Table 1. First-order moment W_1 of the C IV λ4658 emission line and observed heliocentric radial velocities (unit = km s^{-1}) of selected absorption lines as a function of the HJD. The velocities were computed on the basis of the adopted effective rest wavelengths which are given in the header. The selected lines are: the important Ca II K interstellar line (used later on as reference), the four best lines for radial velocity measurements ordered by decreasing wavelengths (see Section 4.1.2), two additional important lines of interest, similarly ordered, as well as the unidentified line near λ4501. The last two columns give V4, a radial velocity resulting from the combination of the above mentioned four best lines and the phase, both derived as described in Section 4.1.2. The variations of the radial velocities of the Ca II K line are also discussed in Section 4.1.2. The wavelength associated to the unidentified absorption near λ4501 is arbitrary.

HJD (2450000+)	W_1 x10	Ca II K 3933.664	He II 4541.59	Hγ 4340.468	He II 4199.83	H8 3889.051	He II 4685.682	Hδ 4101.737	Un.4501 4501.945	V4	Phase
182.687	0.484	3.8	0.0	−27.3	17.0	4.3	36.4	−49.4	−9.1	−16.5	0.711
205.680	0.650	4.1	12.2	−21.3	4.2	−11.1	63.2	−39.0	9.4	−19.4	0.688
206.705	0.350	9.5	30.6	−17.2	16.8	−3.0	45.5			−13.9	0.910
207.676	−0.431	3.0	45.4	36.2	70.7	51.7	75.9	13.3	4.6	36.8	0.120
208.673	−0.249	4.9	48.5	38.9	43.6	40.6	43.2	19.4		26.8	0.336
209.675	0.448	13.0	52.4	7.6	−9.7	15.1		−23.9	16.6	−7.8	0.553
210.669	0.547	6.5	28.5	−32.8	6.9	3.3	59.2	−56.3	−17.8	−16.2	0.768
211.682	0.030	−3.8	26.0	−58.9	9.6	20.5	28.5	−22.7	−10.9	−8.1	0.987
534.697	0.322	15.1	13.0	−9.0	46.9		27.3	−30.8	40.1	−2.7	0.914
534.791	0.239	−2.8	4.7	−25.0	2.6		37.0	−72.9	−37.3	−6.6	0.934
535.690	−0.512	17.3	78.1	17.0		69.9	42.6	35.9	6.2	27.4	0.129
535.779	−0.614	−4.0	56.0	17.4	47.8	54.4	59.8	2.1	6.8	36.7	0.148
536.698	−0.292	10.0	63.8	28.1	41.3	58.4	−35.7	21.7	−2.3	26.7	0.347
536.781	−0.253	3.6	58.5	14.8	50.1	63.9	−5.9	20.1	11.6	32.1	0.365
537.669	0.452	25.6	43.1	6.6	22.8	25.2	27.3	0.1	11.4	−12.4	0.557
537.772	0.429	2.2	26.5	−15.9	−6.8	10.3	32.4	−9.9	2.8	−9.8	0.579
538.686	0.403	14.3	−1.9	−30.1	−14.7	39.3	58.6	−61.9	19.2	−27.3	0.777
538.782	0.369	18.1	2.0	−31.6	9.1	18.7	37.3	−52.0	−9.3	−29.7	0.798
539.698	−0.061	18.8	30.2	2.1	30.7	44.1	28.1	−12.1	20.6	−3.2	0.996
539.798	−0.302	10.5	30.1	5.7	36.7	38.7	−9.4	−2.2	2.1	6.0	0.018
1323.495	0.589		6.1	−10.6						−15.3	0.673
Mean		8.5	31.1	−5.0	22.4	30.2	34.3	−16.9	3.6	0.2	
s.d.		8.2	23.1	25.5	23.6	24.4	27.2	32.1	17.0	21.6	

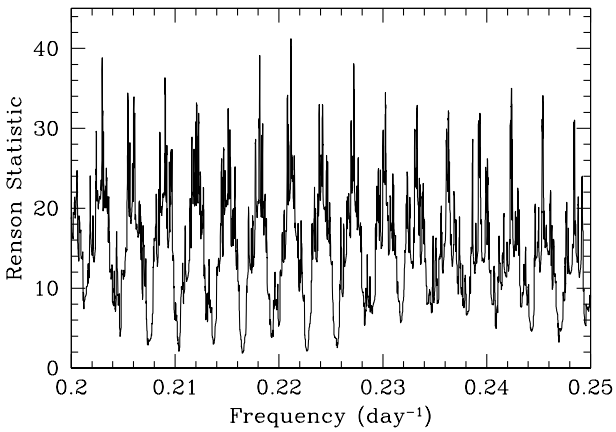

Figure 7. Run of Renson's statistic, for the W_1 time series, as a function of the frequency expressed in d^{-1}. A dip corresponds to a possible periodicity. The region exhibited here is restricted to the central part of the main 1-d alias (the frequency scale is expanded by a factor of 100 compared to the case of Fig. 5). The region is highly structured as a result of the 1-yr aliasing. The deepest dip is at $\nu = 0.2165\,\mathrm{d}^{-1}$ but the ambiguity among the different 1-yr aliases is strong. The low value of the statistic (compared with the continuum which is around 90) indicates a highly significant detection.

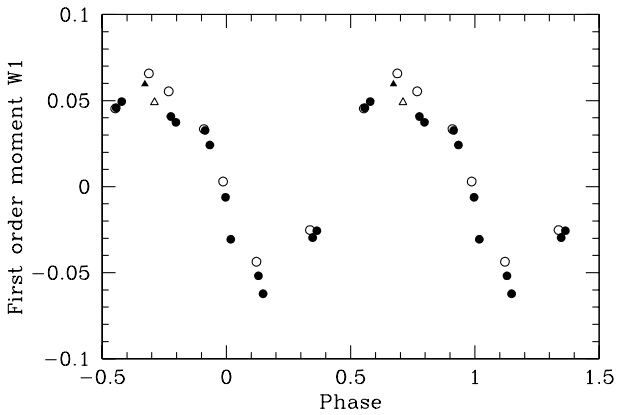

Figure 8. Phase diagram ($P = 4.619$ d) of the first-order moment W_1 of the C IV λ4658 broad emission line. Open symbols are for the 1996 data (triangle: the exploratory spectrum; circles: the 1996 run). Filled circles are for the 1997 data whereas the filled triangle corresponds to the 1999 CTIO spectrum. Both triangles are relevant to spectra separated by more than 3 yr. The stability of the line shape at a fixed phase is remarkable.

observations on the other nights would have definitively solved the problem of the aliasing ambiguity. Nevertheless, waiting for further information, we are rather confident in the choice of the progenitor of the family and we adopt for WR 30a a frequency $\nu = 0.2165\,\mathrm{d}^{-1}$ corresponding to a period $P = 4.619$ d. Provided the right alias has been chosen, we estimate the error in the period to be $\sigma = 0.002$ d. Fig. 8 exhibits a plot of the phase diagram of the W_1 values made with the adopted period. It is clear that the data are consistent from one year to the next. Taking into account the two further spectra (the exploratory one from 1996 and particularly the spectrum from 1999 at CTIO), we can conclude that WR 30a exhibits periodic emission-line profile variations and the recurrence of the line profiles has been stable over a span of time of 3 yr.

4 ANALYSIS OF THE SPECTRUM OF WR 30a

4.1 The absorption spectrum

4.1.1 The spectrum of the O component

The spectrum of WR 30a is illustrated in Fig. 4 where the

Table 2. Identification of the non-WO lines in the composite spectrum of WR 30a and measured equivalent widths as compared to those published by Kingsburgh et al. (1995). When necessary, the equivalent widths have been corrected for the extra light because of the presence of the broad emission lines.

Line	Position (Å)	Eq. Width (Å) Kingsburgh et al.	Eq. Width (Å) This work
H9 + He II λ3834	3836	0.47	0.80
He II λ3858	3860		0.24
H8 + He I λ3889+He II λ3887	3890	1.43	1.26
He II λ3923	3924		0.34
Ca II K (IS)	3934	0.95	0.94
Ca II H (IS) + Hϵ	3969	2.43	1.96
He I λ4026 + He II λ4026	4026	0.74	0.39
Hδ + He II λ4100	4102	1.48	1.89
He II λ4200	4200	0.75	0.54
Hγ + He II λ4339	4340	1.70	1.79
DIB λ4430	4427	4.72	4.90
He I λ4471	4472	(0.2)	0.19
Mg II λ4481	4481		0.08
? (b)	4495		0.06
Un.λ4501	4502		0.28
He II λ4542	4542	0.80	0.76
N III λ4634	4635		E
N III λ4641	4641		E
He II λ4686	4686		0.36
DIB λ4727 (a)	4728		0.29
DIB λ4763 (a)	4763		0.20
DIB λ4780 (a)	4780		0.10

E : in emission; (a) Cami et al. (1997); (b) possibly present, could also be present in the O4-5((f)) star HD 46223 Morrell, Walborn & Fitzpatrick (1991), N IV λ4495?

composite spectrum is displayed along with the identification of the lines (more details are available in Table 2). We measured the equivalent widths in both mean spectra. No discrepancy between 1996 and 1997 is apparent and the resulting values are available in Table 2 along with those measured by Kingsburgh et al. (1995). Our values have been corrected for the effect of the WO emission lines when necessary. WR 30a exhibits prominent absorption lines of hydrogen and helium belonging to the hot O star companion. The interstellar Ca II K line is clearly visible and the diffuse interstellar band (DIB) at λ4430 is particularly strong. The strength of the line at λ4501 is also remarkable. Scholz (1972) observed this line in absorption in 9 Sgr and HD 54662, but gave no identification. Herbig (1995) reported the existence of a DIB at this position.

Since the lines He II λ4542 and He I λ4471 are determinant for the classification of early O stars, we paid particular attention in measuring their equivalent widths in every individual spectrum in order to check their stability with time. The equivalent width of the He II line is easily measurable; its mean value is W(He II λ4542) = 0.76 Å ($\sigma = 0.06$ Å), and no variation shows up with the phase of the 4.619-d period. This value is in perfect agreement with the one measured in the composite spectrum [W(mean He II λ4542) = 0.76 Å]. The He I line is much more difficult to address, and indeed we have been unable to measure it on a few individual spectra. The mean equivalent width over the different individual spectra, for which we have been able to perform a fit, is W(He I λ4471) = 0.26 Å ($\sigma = 0.07$ Å). No systematic trend has been found with the period. However, since this line could not be measured when it was too weak, this value for He I λ4471 is biased and should be considered as an upper limit. The related value on the composite spectrum is W(mean He I λ4471) = 0.19 Å. It should be more accurate and less biased since all the suitable spectra are fully involved in its determination. Conti (1973b) defined the classification criterion W' as the ratio of the equivalent widths of the two helium lines: $W' = W$(He I λ4471)/W(He II λ4542). From the mean of the individual values of the Ws, we compute $W' = 0.34 \pm 0.09$ ($\log W' = -0.47$) corresponding to an O5.5 star whereas the ratio of the values deduced from the mean spectrum, $W' = 0.25$ ($\log W' = -0.60$), points to an O5 type. We adopt this latter classification which is slightly cooler than the usually admitted O4 type. On the basis of our spectra, it is not possible to deduce a luminosity class. The only indication we have is the presence of the line He II λ4686 markedly in absorption which suggests that the star is certainly not a supergiant. Mathys (1988) suggested the use, for hot O stars, of a luminosity criterion based on the absolute equivalent width of the He II λ4686 line. Accordingly, a main-sequence star is expected to have an equivalent width larger than $W = 0.56$ Å, whereas the equivalent width would be reduced through emission filling in the profile in a giant star. The observed equivalent width for WR 30a, $W = 0.36$ Å, is markedly too small for a main-sequence star (even accounting for a dilution by the WO continuum, see below) and would rather suggest a giant.

The equivalent widths related to the O star, as measured above, should be systematically diluted by the continuum light coming from the WO component. We can try to have an idea of the visual brightness ratio around $\lambda = 4400$ Å, $q = L_{4400,\mathrm{WO}}/L_{4400,\mathrm{O}}$, by measuring the dilution effect. Indeed, the observed equivalent width can be expressed as a function of the intrinsic one of a single star (of a given spectral type) by

$$W_{\mathrm{obs}} = W_{\mathrm{sing}} \frac{1}{1+q} \tag{4}$$

and therefore

$$q = \frac{W_{\mathrm{sing}}}{W_{\mathrm{obs}}} - 1. \tag{5}$$

Table 3. Comparison of the equivalent widths (unit = Å) observed in WR 30a with those found in the literature for stars of spectral types O4, O5, O5.5 and the mean over the three types. The corresponding visual brightness ratio q (from equation 5) is given in italics. Negative values correspond to a measured W_{obs} larger than the average value expected for a single star. This could be because of either a large uncertainty in the W_{sing} values or an unsuitable spectral type.

Line	W_{obs}	W_{sing}			
		O4	O5	O5.5	O4 to O5.5
He II λ4542	0.76	0.80	0.84	0.81	0.81
		0.050	*0.099*	*0.070*	*0.071*
Hγ	1.79	1.63	2.06	1.85	1.84
		−0.089	*0.148*	*0.034*	*0.028*
He II λ4200	0.54	0.54	0.51	0.55	0.55
		0.002	*−0.052*	*0.011*	*0.011*

We will restrict ourselves to the strongest lines in order to avoid spurious results because of the poor quality of the determination of the observed equivalent widths. Four lines fit this criterion: He II λ4542, Hγ, He II λ4200 and He II λ4686. Nevertheless, the latter has been disregarded, not only because it is well known for its propensity to develop emission but also because it is located atop a strong variable emission. We deduced the W_{sing} value from the paper of Conti (1973a) by computing average values of the equivalent widths of these lines as a function of the three spectral types of interest here (O4, O5, O5.5). We also computed the joint mean over the three spectral types. The results of this analysis are given in Table 3. It is immediately clear that the dispersion of the q values is rather large. Nevertheless, q is certainly less than 0.1 and most probably around 0.04 (from the average over the last column). This means that the WO component is some 2.5 or 3.5 mag fainter than the O star in the continuum around $\lambda = 4400$ Å. This 1-mag uncertainty encompasses the difference in brightness between a WO and any of the two luminosity classes, main sequence or giant. In any case, this level of dilution is not sufficient to change the conclusions we drew from the application of the Mathys criterion for deriving the luminosity class of the O star.

An inspection of Fig. 4 shows that two narrow emission lines seem to be present in the composite spectrum around 4640 Å. These two narrow lines can be identified with the N III λλ4634–4641 lines. Because of their width, they cannot be linked to the WO component and they are necessarily attributable to the O5 star or to some matter elsewhere in the system. The presence of the N III λλ4634–4641 lines is not unusual in O5 stars (see e.g. Walborn & Fitzpatrick 1990). However, in the present case, they are usually extremely difficult to detect in the individual spectra in general but are sometimes clearly present. This is particularly the case in the spectrum of HJD 245 0205.7 (see Fig. 3, left panel). Combined with the aspect of the He II λ4686 line, this detection suggests an O5((f)) classification for the companion of the WR.

4.1.2 The orbital motion of the O component

We tried to detect the orbital motion of the O star. For most of the well-defined lines, we measured their positions by fitting a Gaussian function to the line profile. These positions have been converted into radial velocities using the effective rest wavelengths compiled by Conti, Leep & Lorre (1977) and Underhill (1995). Table 1 gathers the results and gives the heliocentric radial velocities as a function of the HJD for the main lines. Mean and standard deviations are also available. Hε was disregarded because it is biased by the presence of the interstellar Ca II H line. The dispersion among the velocities of the Ca II K line gives an idea of the precision reachable on a strong narrow line. In the 1997 data, we find a systematic difference in velocities between the first and the second spectrum of each night ($\Delta v \sim 12.3\,\mathrm{km\,s^{-1}}$, $\Delta t \sim 0.095$ d). This difference is certainly indicative of flexure in the spectrograph and, in further treatment, we will refer the radial velocities of each observation to the one of the Ca II K line in order to perform a first-order correction to this problem. The spectrum from CTIO cannot be corrected this way: the Ca II K line is not covered by this spectrum.

Among the lines of interest is He II λ4686. Unfortunately, this line is superimposed on the broad C IV λ4658 blend of the WO component which is a strongly variable feature. It is obvious that the measured position of He II λ4686 may be affected by the particular shape of C IV λ4658 at that time. In order to obtain access to this line we used a particular method. Each spectrum has been decomposed in wavelets (Lépine, Moffat & Henriksen 1996). The continuous wavelet transform of the spectrum $F(x)$ is defined as

$$WT(b,a) = K_g(a) \int_{\mathcal{R}} F(x) g\left(\frac{x-b}{a}\right) \mathrm{d}x \tag{6}$$

where we use as the real mother wavelet the so-called Mexican Hat (basically the second derivative of the Gaussian)

$$g(v) = (1 - v^2) \exp\left(-\frac{v^2}{2}\right), \tag{7}$$

and where $K_g(a)$ is a normalization constant which takes the value $1/\sqrt{a}$ for the adopted g. b has the nature of a position over the spectrum (as x) and a (≥ 0) has the nature of a typical scale (or spatial frequency). Then, we compute the normalized wavelet transform

$$NWT(x,a) = \frac{1}{C_g} K_g(a) \int_{\mathcal{R}} WT(b,a) g\left(\frac{x-b}{a}\right) \frac{\mathrm{d}b}{a} \tag{8}$$

where C_g is another normalization constant taken here to be equal to π. In this normalized wavelet transform, the variations at a fixed a value (a fixed scale) are directly comparable to the variations in the spectrum compatible with this frequency. Finally, we can recover the original spectrum by making a last integration

$$F(x) = \int_0^\infty NWT(x,a) \frac{\mathrm{d}a}{a}. \tag{9}$$

It is clear that, if we limit the interval over which the last integration is made, we use some kind of filtering according to the scale. In the present case, we reconstructed the spectra limiting ourselves to the 'frequencies' higher than a typical scale of 3.75 Å. This is equivalent to removing the low frequencies and, indeed the C IV λ4658 line, essentially composed of low frequencies, is filtered out by the process. The selection of the typical scale $a =$ 3.75 Å is somewhat arbitrary. We took the smallest value that allows a good reconstruction of isolated lines such as He II λ4542.

In Fig. 9, we show the line profile of C IV λ4658, as observed in our exploratory spectrum of April 1996, along with the corresponding reconstructed spectrum. The He II λ4686 line of the O star is easily spotted. We measured the positions of this line on such reconstructed spectra in order to get rid of the effect of the WO line. A word of caution is necessary here: as will appear in Section 4.2.2, the WO line contains also intrinsically high frequencies (i.e. small-scale structures) and we are certainly

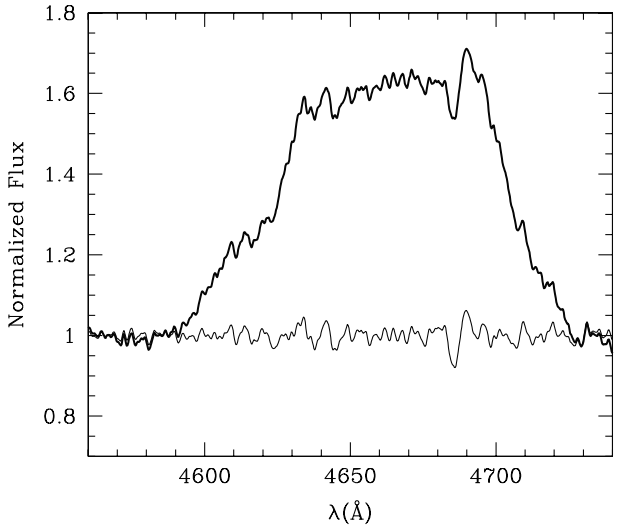

Figure 9. The exploratory spectrum of 1996 April (HJD 245 0182.7) in the region of the C IV line (thick line), along with the spectrum reconstructed by integrating the normalized wavelet transform up to scales of 3.75 Å only. The measurement of the position of the He II λ4686 absorption by fitting a Gaussian profile is more accurate on the reconstructed spectrum which has the advantage of being free from heavy slopes as illustrated here. On both versions of the exploratory spectrum, the He II λ4686 line associated to the O star exhibits a P Cygni profile.

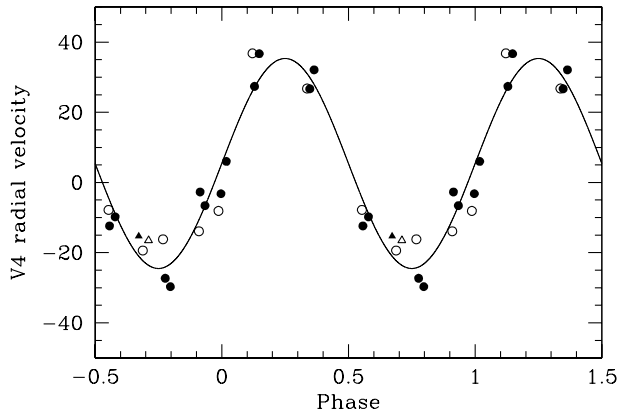

Figure 10. Phase diagram ($P = 4.619$ d) of the V4 radial velocities (km s^{-1}) which are associated with the motion of the O star. The symbols are the same as in Fig. 8. Both triangles are relevant to spectra separated by more than 3 yr. The continuous line represents the theoretical velocity curve that has been fitted to the data assuming a circular orbit and the period derived in Section 3. The O star is in front at phase zero which corresponds to $T_0 =$ HJD 245 0535.095.

limited by these high frequencies even when using the wavelet filtering. Nevertheless, thanks to this method, we succeeded in getting rid of the effect of the low frequencies.

We inspected the radial velocities of all the O-star absorption lines as a function of the period. All the lines exhibit a periodic motion with a very similar amplitude, which underlines the orbital movement. The only exception is the unidentified line at λ4501 which does not seem to participate in the orbital movement. It should also be noticed that the dispersion of the measurements of this line is inferior to what is observed for the other stellar lines ($\sigma = 17.0$ km s^{-1} against about 25 km s^{-1}). This line is probably stable in velocity and this latter standard deviation gives an idea of the worst precision we have on faint lines. It is very likely that this line is essentially of non-stellar origin and could be assimilated with the DIB at $\lambda = 4501.8$ Å (Herbig 1995; Cami et al. 1997). The strength of the band is fully compatible with those of the DIBs at λ4430 and at λ4727, the three lines here having equivalent widths 45 to 50 per cent larger than in HD 183143 (Herbig 1995).

The He II λ4686 line, made accessible thanks to the wavelet filtering, follows rather accurately the He II λ4542 variations except at HJD 245 0182.7 and 245 0205.7 where the absorption components are apparently shifted to the blue. The agreement between the radial velocities of these two He II lines was not satisfactory before we filtered out the WO line.

As a matter of fact, weak lines are more difficult to measure. Therefore, some lines are much more suited to outline the motion of the O star. We selected four lines, namely He II λ4542, Hγ, He II λ4200 and H8, that we consider to form the best set for studying the orbital motion (again, the He II λ4686 line was not included because of its above mentioned particular behaviour at HJD 245 0182.7 and 245 0205.7). It is necessary to recall here that the velocities we used are referred to the Ca II K line. The following procedure has been applied: we first calculated, for each spectrum, the velocity of the different lines relative to their respective means (i.e. the mean as given at the bottom of Table 1 corrected by the mean for the Ca II K line). We then computed, for each spectrum, the velocity labelled V4 which is the mean over the four lines of these relative velocities. Missing measurements have been either neglected or replaced by an estimated value for the calculation of the mean. V4 is expected to be representative of the mean motion of these four lines and hence of the orbital motion (although its zero-point has no particular meaning).

We adjusted a sine curve with the period derived in Section 3 to these V4 velocities. The use of higher harmonics turned out to be unnecessary, suggesting a circular orbit. Therefore, the fitted amplitude gives the orbital velocity constant $K_O = 29.9$ ($\sigma = 2.1$) km s^{-1}. The time of conjunction of the system with the O star in front of its companion is deduced from the phase of the sine and is $T_0 =$ HJD 245 0535.095 ($\sigma = 0.049$). The fitted radial velocity curve is displayed in Fig. 10 along with the data. Phase zero of the system is taken to correspond to the conjunction at T_0. According to this definition, the actual phases corresponding to the individual spectra are given in Table 1. From Fig. 10, it is immediately clear that the orbit is circular (or very nearly so) which we will admit hereafter. We can now derive the mass function as well as the projected size of the orbit: $f(m) = 0.013$ ($\sigma = 0.003$) $M_\odot$ and $a_O \sin i = 1.96 \times 10^6$ ($\sigma = 0.13 \times 10^6$) km $= 2.8\,R_\odot$. If we adopt the mass for an O5 star published by Howarth & Prinja (1989; 58 $M_\odot$ for a main-sequence star and 68 $M_\odot$ for a giant), we deduce from the mass function a minimum mass of $M_{WO} = 3.6\,M_\odot$ or, respectively, $4\,M_\odot$. A conservative approach attributing a mass of 35 $M_\odot$ to the O star gives a minimum mass of 2.6 $M_\odot$ for the WO.

A caveat is necessary here. The errors quoted above are derived from the quality of the fits. Although it is clear that the movement of the lines in radial velocity is a first-order effect, the limited S/N ratio of our spectra does not allow us to rule out the existence of line-profile variations. This would not be too surprising since Niemela (1995) reported the existence of a Balmer progression. This conclusion is not contradicted by our mean radial velocities as given in Table 1. A Balmer progression is a sign that the hydrogen absorption lines are formed in an expanding atmosphere. The mere presence of this effect may induce line-profile variations. More generally, some of the hot O stars are suspected or known to exhibit non-radial pulsations: another factor influencing the line profiles.

Therefore, the existence of line-profile variations, even if it is a secondary effect, can possibly affect the radial velocity measurements and thus the above mentioned results. Only higher S/N and higher resolution data could give a definitive answer to this question. The peak-to-peak variations as deduced from the fig. 2 of Niemela (1995) range from about -40 to about $60\,\mathrm{km\,s^{-1}}$; this is 67 per cent larger than the value we observe.

On HJD 245 0182.7 (see Fig. 9), the He II λ4686 line develops a weak P Cygni profile. The P Cygni width is narrow enough to allow its dissociation from the WO line by wavelet filtering. This spectrum corresponds to phase $\phi = 0.711$ and, as mentioned above, the absorption component is somewhat shifted to the blue. This latter characteristic is also shared by the spectrum on HJD 245 0205.7 which turned out to correspond to the same phase ($\phi = 0.688$). It should be recalled that HJD 245 0205.7 is also the time when the N III $\lambda\lambda$4634–41 lines are best seen. These different phenomena seem to be rather restricted in phase at $\phi = 0.7$.

4.2 The broad emission spectrum

Only two broad lines, typical of WR stars, are outstanding in the domain covered by our observations. The strongest one, labelled C IV λ4658, is actually a blend of several spectroscopic lines: C IV λ4658 (6–5), C IV λ4685 (8–6), C III $\lambda\lambda$4647–4650 (3–3) and He II λ4686 as well as, less vigorously, C IV λ4647 (6–5), C IV λ4689 (11–7) and O VI λ4678 (see Torres & Massey 1987; Kingsburgh et al. 1995; Crowther et al. 2000). The second one is the doublet O VI $\lambda\lambda$3811–34 at the blue edge of the domain. We measured for C IV λ4658 an equivalent width of -52 Å in our spectra; the agreement with the value (-62 Å) of Kingsburgh et al. (1995) is only marginally good. The equivalent width of C IV λ4658 is not perfectly constant but presents 6 per cent peak-to-peak variations. This is locked in phase with a maximum of emission around phases $\phi = 0.1$ and 0.6. Compared with its strength in the spectra of other WR stars of similar subtype, the broad C IV λ4658 emission line turns out to be relatively faint in the spectrum of WR 30a. This could be because of the dilution by the light of the O component that artificially increases the level of the continuum. According to this point of view, we can use this effect to get another estimate for q. Very few reliable measurements exist, but, if one adopts, for C IV λ4658, the same intrinsic equivalent width as for the presumably single WO4 star Br93 ($\log W = 2.73$, Conti & Massey 1989), we obtain

$$q = \frac{W_{\mathrm{obs}}/W_{\mathrm{sing}}}{1 - (W_{\mathrm{obs}}/W_{\mathrm{sing}})} \sim 0.1 \qquad (10)$$

in reasonable agreement (neglecting the slight difference between both wavelength domains) with the value deduced from the dilution of the absorption lines (Section 4.1.1). If one prefers some mean value drawn from the WC4 population (without absorption lines) in the Galaxy (only one reliably measured object: WR 38 giving $\log W = 2.78$, Conti & Massey 1989) or in the Large Magellanic Cloud (LMC) ($\log W = 2.94$, Conti & Massey 1989), one gets $q = 0.09$ and 0.06, respectively. In the meantime, some of these stars have been reclassified, and Br93 has now been assigned a WO3 spectral type (Crowther et al. 1998).

4.2.1 Search for the orbital motion of the WO component

The C IV λ4658 emission line exhibits variations that essentially concern the shape of the line. In particular, the top of the profile is continuously changing by large amounts. In this respect, it is easily understandable that the detection of a possible orbital movement is difficult, even if these variations are periodic and deterministic (as shown above). The first approach we adopted was to measure the positions of the wings of the line. The level above the continuum at which we can operate is critical: if too high, the result is dominated by the line-profile variations, and, if too low, it is dominated by the inaccuracies in the continuum adjustment. We chose to perform the measurements at 15 per cent above the normalized continuum. The resulting radial velocities are given in a phase diagram, both for the red wing and for the blue wing in Fig. 11. It is evident that the wings are moving in antiphase with the O star and this is a good argument to conclude that we are indeed observing the orbital motion of the WO component. From the data shown in Fig. 11, we can deduce apparent orbital velocities of $K_{\mathrm{red}} = 189$ and $K_{\mathrm{blue}} = 286\,\mathrm{km\,s^{-1}}$. The two values are significantly different, which is a problem.

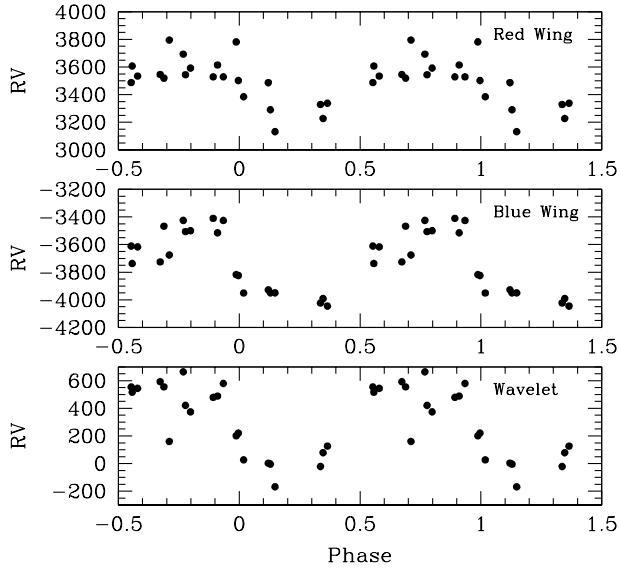

Figure 11. Phase diagram ($P = 4.619$ d) of the radial velocities ($\mathrm{km\,s^{-1}}$) associated to different parts of the C IV line of the WO component (see text for details). Upper panel: red wing at 15 per cent over the normalized continuum. Middle panel: blue wing at 15 per cent over the normalized continuum. Lower panel: central velocity measured on the normalized wavelet transform at a scale $a = 125$Å. The velocities of the two upper panels are essentially opposite in phase with respect to the O star. The curve in the lower panel presents a small shift in phase (to the left).

We also adopted another method. The profile variations are so strong and the shapes so particular that it is illusory to try to fit a Gaussian to the line in order to derive an accurate position. However, the idea of using the whole profile (instead of the wings alone) sounds basically good. We therefore decided to measure the position of the maximum related to C IV λ4658 in the normalized wavelet transform of the spectrum. We selected the wavelet of scale $a = 125$ Å. This large scale has the advantage of being comparable with the global line width and, consequently, the line-profile variations are implicitly integrated and attenuated when computing the normalized wavelet transform. The lower panel of Fig. 11 gives the results corresponding to this method, which leads to an apparent orbital velocity $K_{\mathrm{wav}} = 303\,\mathrm{km\,s^{-1}}$. This radial velocity curve is slightly out of phase ($\Delta\phi = 0.04$) with respect to the antiphase of the O star. It is interesting to note that the value of

$K_{\rm wav}$ is in good agreement with the range of values (-100, $520\,{\rm km\,s^{-1}}$) covered by the data of Niemela (1995). Nevertheless, the line-profile variations that strongly modify the top of the line are certainly playing a rôle in the determination of the global position. As will be shown in Section 4.2.2, the line-profile variations appear to be out of phase with both the O and the WO component. The phase shift observed in the results of the wavelet method could indicate that these line-profile variations do have a small influence. The net effect of putting no constraint on the phase of the fitted sine curve is to boost the fitted $K_{\rm wav}$ to larger values. Therefore $303\,{\rm km\,s^{-1}}$ should be considered as an upper limit on the value of $K_{\rm WO}$. Being in antiphase with the O star, the wings can certainly be more reliable. The possible presence, in the blue wing, of absorption components (e.g. of P Cygni profiles) blended with the overall emissions, is an argument against its use as a radial velocity indicator since the absorption component can be variable. We will present another argument in the next section. On the contrary, the red wing should not be strongly vitiated. Therefore, we consider that the best estimate for the orbital motion constant comes from the red wing. We thus associate to the orbital velocity of the WO component $K_{\rm WO} = 189\,{\rm km\,s^{-1}}$ with the possibility that the actual value could be larger by up to 60 per cent. This result should be confirmed by the observation of other lines that would be less affected by line-profile variations.

One of these lines could have been O VI λλ3811–34, but, in our set of spectra, the doublet is too much corrupted by the absorption lines of the O companion to allow any meaningful measurement. It would be interesting to investigate other wavelength domains in order to find lines more representative of the orbital motion.

A value $K_{\rm WO} = 189\,{\rm km\,s^{-1}}$ gives $a_{\rm WO}\sin i = 12\times10^6\,{\rm km} = 17.2\,{\rm R_\odot}$ and a mass ratio for the system $M_{\rm WO}/M_{\rm O} = 0.16$. This value is in good agreement with the value 0.2 typically proposed (Moffat, Niemela & Marraco 1990) for O + WC4/WO4 systems. The same authors give for SMC AB8 (WO4 + O7) a mass ratio of 0.27. From Howarth & Prinja (1989), we can deduce a factor of about 1.65 between the mass of a typical O5 star and a typical O7 star. From these two values, we can estimate the mass ratio for a WO4 + O5 system and we find 0.16, in perfect agreement with the value we derived for WR 30a. This mass ratio implies $M_{\rm WO}\sin^3 i = 0.69\,{\rm M_\odot}$ and $M_{\rm O}\sin^3 i = 4.34\,{\rm M_\odot}$.

No trace of mutual stellar eclipse is seen in the photometry. Therefore we can derive an upper limit on the inclination angle of the system. If we conservatively adopt a radius $R_{\rm O} = 10\,{\rm R_\odot}$ and a point-like source for the WO star, we obtain $i \leq 63°$ which is not extremely constraining. Adopting a mass for the O star of $68\,{\rm M_\odot}$ ($58\,{\rm M_\odot}$ and $35\,{\rm M_\odot}$, respectively) leads to a mass for the WO component of $10.8\,{\rm M_\odot}$ ($9.2\,{\rm M_\odot}$ and $5.5\,{\rm M_\odot}$, respectively) and to a possible inclination of, respectively, 23°.6, 25°.0 and 30°.3. This inclination angle is only weakly dependent on the hypotheses made about the masses.

4.2.2 *Broad emission-line profile variability*

We are now going to investigate the profile variations of the C IV line. In order to emphasize the variability of a WR line profile, it became a classical approach to remove the mean profile. This technique has usually been efficient (see e.g. Vreux et al. 1992) and instructive as long as one keeps in mind that the mean profile is not an absolute, physically meaningful, reference and that, for example, a deficit in the residual spectrum does not necessarily imply an absorption (and vice versa). In the case of WR 134 (Vreux et al. 1992), the nice symmetric mean profile of the He II lines was very encouraging. In the present case, the mean profile of the C IV line (see Fig. 4) clearly indicates that this technique is not necessarily recommended. Actually, the distribution in phase is not uniformly random enough with respect to the variability; the mean profile is dominated by some particular realizations and is thus statistically inhomogeneous over its width. Although with the same above mentioned caveats, we instead tried to define a maximum, smooth and symmetric profile that underlines all the observed shapes of the C IV line. Although all the profiles participate in the definition, the most constraining ones are certainly those observed around phase 0.55. At that time, the part of the profile that is not at the minimum emission is the most restricted in wavelength. Fig. 12 shows two of these profiles (which by the way are quasi-identical although they are separated by 1 yr) as well as the parabolic line that best corresponds to our quest. Indeed, the parabola turned out to be the symmetric function giving the best overall fit to the profiles as is easily seen in Fig. 12. It is interesting to note that this parabolic line is well centred on C IV λ4658 and has a derived width of 140 Å, in very good agreement with the terminal velocity ($4500\,{\rm km\,s^{-1}}$) proposed by Kingsburgh et al. (1995). Using this template, we thus separated the observed profile into two parts: a basic line with a parabolic shape and an almost rectangularly shaped region with what appears as extra emission (apparent extra emission, AEE). Again, we have to keep in mind that this partitioning is not necessarily physically meaningful: the use of the qualificative 'apparent' in AEE is a reminder. The profile at $\phi = 0.55$ (in Fig. 12) corresponds to a phase where the WO star just passed in front of the O star. Therefore, if we had the desire to increase the intensity of the basic line (while keeping its symmetry), we would have to admit that the spectra of Fig. 12 must present an extra absorption in the domain 4620–4640 Å. Since this domain corresponds to matter in the part of the wind between the WR and us, it is difficult to imagine any process which is able to act in this way other than absorption of the background light by the WO wind. It remains unclear whether the wind opacity in this transition is sufficient to produce such a selective atmospheric eclipse.

We adopted the basic parabolic line illustrated in Fig. 12 and we subtracted this basic profile from all the observed C IV lines. In the

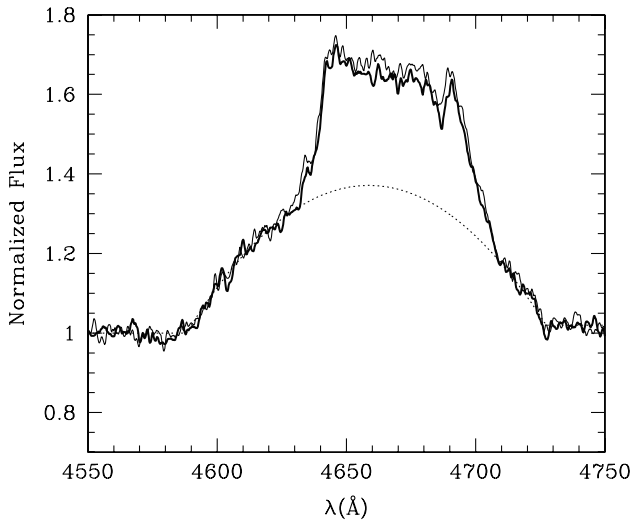

Figure 12. The spectrum of WR 30a around the C IV line at phase $\phi = 0.553$ (1996, thick line) and 0.557 (1997, thin line). The similarity between both spectra is particularly visible here. We also plotted the parabolic basic line profile that we chose as a reference.

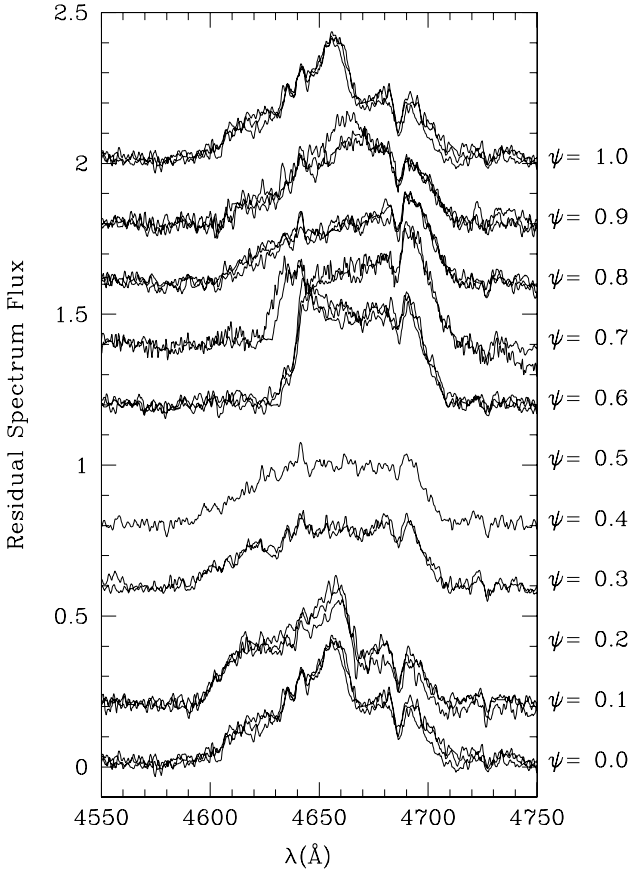

Figure 13. The residual spectra resulting from the removal of the parabolic component. The spectra have been shifted upwards as a function of the phase bin they belong to. The shift is 0.2 intensity unit for a change in binned phase of 0.1. All the spectra within one phase bin are plotted at the centre of the bin. The value of the binned phase ψ is given as a label.

process, we took into account the orbital motion of the WO component, as deduced in the previous section, in order to shift the profile adequately. The resulting residual profiles are however almost insensitive to the orbital motion correction. In order to illustrate the line-profile variability, we plot the residual profiles in Fig. 13: they have been shifted upwards according to their phase. For the sake of clarity, we further decided to bin the phases in steps of 0.1 centred on 0.0, 0.1, 0.2, and so on. All the residual spectra belonging to a phase bin have been plotted at the centre of the bin: this has the advantage of a much clearer picture. The dominant discrepancies between spectra in the same phase bin are because of the deterministic variations within one tenth of the period.

The residual spectra corresponding to the profiles shown in Fig. 12 ($\phi = 0.553$ and 0.557) are in Fig. 13 at the binned phase $\psi = 0.6$. At this phase, an AEE is located in the 4640–4700 Å range and is flanked with well-defined edges. When going from binned phase $\psi = 0.6$ to 0.7, the AEE which had a flat (or slightly inclined to the red) top evolves into a similar feature inclined to the blue and with a wing extending further to the blue down to 4630 Å at phase $\phi = 0.688$, and to 4625 Å at phase $\phi = 0.711$. At binned phase $\psi = 0.8$, the blue extension evolves into a fully smooth and continuously decreasing feature up to 4605 Å. In the meantime, the intensity of the red part has slightly decreased. At $\psi = 0.9$, the red part still decreases whereas some additional AEE appears between 4640 and 4670 Å. In the last spectrum belonging to $\psi = 0.9$ ($\phi = 0.934$), a stronger increase of intensity is visible between 4655 and 4665 Å. The latter maximum seems to have shifted to 4655 Å at $\psi = 0.0$. A steep wing appears at 4665 Å and an AEE extends now from 4595 to 4660 Å. At $\psi = 0.1$, the AEE between 4595 and 4660 Å markedly strengthens and reaches a maximum generating an edge on its blue side. AEE in the range 4665–4700 Å persists. Actually, we have no spectrum around phase 0.05, i.e. half a period later than the spectra of Fig. 12. Binned phase $\psi = 0.1$ is populated by the spectra at phases $\phi = 0.120$, 0.129 and 0.148. The last spectrum before $\psi = 0.1$ is at phase $\phi = 0.018$. Nevertheless, it is interesting to note that the bluewards shifted AEE (BAEE) at $\psi = 0.1$ is very similar to the redwards shifted one (RAEE) at $\psi = 0.6$ (actually $\phi = 0.553$ and 0.557). This BAEE at binned phases 0.0 and 0.1 extends sufficiently bluewards to have a strong influence on the position of the blue wing of the entire C IV line. This induces biased velocities that are more negative as can be seen in Fig. 11 (middle panel). This is a second reason to cast doubts about the blue wing velocity as an indicator of the orbital motion of the WO star.

Finally, at binned phases $\psi = 0.3$ and 0.4, the BAEE has disappeared and the profile seems stable for at least one tenth of the period. Still at these phases, some weak AEE is present over the whole domain of the C IV line. In the range bluewards of 4635 Å, this AEE disappears at phase 0.55 ($\psi \sim 0.6$). In the range 4640–4700 Å, this AEE is indeed always present and contributes to the RAEE of phases 0.55–0.56. In other words, this weak persisting AEE (PAEE) seems to constitute a stable component having most probably the same origin as the emission defined by the parabolic line. This would suggest that the C IV line has a stable asymmetric profile which is not surprising for such a complex blend. Therefore, we tried to define an asymmetric basic profile which we subtracted from all the observed profiles. Relaxing the hypothesis of symmetry for the basic (to be subtracted) profile, we were facing several possibilities (or degrees of freedom) in its definition. We decided to create an asymmetric basic profile on the basis of the minimum emission profile. For wavelengths shorter than 4630 Å, the minimum profile is actually defined by the profile at $\psi = 0.6$, whereas for wavelengths longer than 4670 Å, it is set by the profile at $\psi = 0.1$ thus including the PAEE. In the range 4630–4670 Å, the profile actually remains undefined and we decided to interpolate smoothly between the pieces of spectra on both sides. This basic asymmetric profile thus combines the parabolic line and the PAEE. We subtracted it from all the individual spectra, making a new family of residual spectra. Comparison of this new family with the old one, shown in Fig. 13, does not reveal any fundamental difference in the behaviour of the AEEs. Two modifications are nevertheless worth pointing out. At phase $\psi = 0.1$, there is, of course, no longer any AEE to the red of 4670 Å. At phase $\psi = 0.6$, the RAEE sees its intensity reduced by a factor of 2 on its red side. It now exhibits a strong inclination to the red. Indeed, in these new residual spectra, the RAEE is much more similar to the mirrored version of the BAEE. Despite some arbitrariness in the decomposition process of the profile, we advocate that the BAEE and the RAEE, and the symmetry they exhibit, are inescapable features to understand the line-profile variability in WR 30a. In the next section, we tentatively discuss the significance of the variable component of the profile. To support the discussion, we present in Fig. 14 a rough qualitative sketch of the WR 30a system annotated with two selected residual spectra laid out at the projected line of sight corresponding to their phase. The new residual spectra exhibited in Fig. 14 result from the subtraction of the above mentioned asymmetric basic profile.

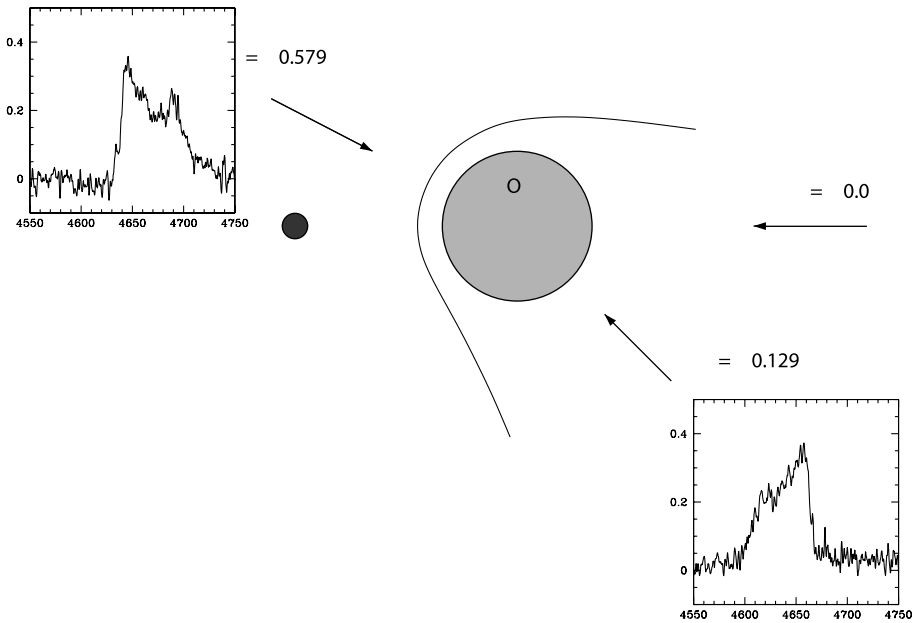

Figure 14. A qualitative sketch of the system of WR 30a seen from outside the orbital plane with the WO4 component (left) and the O5((f)) star. The wind–wind collision interface is schematically drawn; it is slightly tilted to illustrate the effect of the Coriolis force. Phase zero corresponds to the conjunction with the O star in front as shown by the projected line of sight annotated $\phi = 0.0$. Two selected examples of residual spectrum (second family) are inserted in the figure: the abscissae correspond to the wavelength expressed in Å whereas the ordinates give the residual intensity in continuum units. The insets are laid out at a projected line of sight corresponding to their respective phase. The left one is representative of the RAEE, the right one of the BAEE (see Sections 4.2.2 and 5).

5 DISCUSSION

From the study presented above, it is now beyond any doubt that WR 30a is a binary system with a period around 4.6 d. The identification of the components as WO4 + O5((f)) indicates a binary that could be enlightening for massive star evolution. The colours of WR 30a are definitely dominated by those of the O5 component. In a standard $U - B$ versus $B - V$ colour diagram, the observed photometric values of Wramdemark (1976) are fully compatible with an early O star exhibiting a colour excess $E(B - V) = 1.36$. The 15–18 per cent central absorption of the DIB at λ4430 (Herbig 1995) would even suggest a larger extinction but the results of Herbig (1995) might not apply to the Carina line of sight. If we adopt an absolute magnitude of −5.5 (−6.2 respectively) corresponding, according to Howarth & Prinja (1989), to a main-sequence (giant respectively) star with a 10 per cent additional contribution for the WO component, WR 30a should be located at about 6 kpc (8 kpc respectively). No particular well-known feature (e.g. a cluster) is present in this direction and we cannot, for the moment, confidently discriminate between the two luminosity classes. In the last version of the catalogue of galactic WR stars, van der Hucht (2001) derives for WR 30a a distance of 7.8 kpc.

While the radial velocity curve of the O star is rather reliable, the curve for the WO component should still be confirmed by analysing lines other than the C IV λ4658 line. The latter indeed exhibits strong line-profile variability, locked with the orbital phase, that prevents a fully secure measurement of the orbital velocity. At phase 0.553–0.557, i.e. a little after the conjunction with the WO in front, the profile exhibits a strong, mainly redshifted, apparent extra emission (RAEE, see Fig. 12, in the range 4640–4700 Å). It is attributable to emitting matter having projected velocities roughly from 0 up to 2500–3000 km s^{-1}. At that phase, both stars exhibit radial velocities close to the one of the centre of mass which is rather small (typically 30 km s^{-1}). Velocities as large as 3000 km s^{-1} cannot be attributed to an orbital movement: this would necessitate some stable feature at quadrature having such a velocity and remaining gravitationally bound to the system which is dynamically impossible. On the contrary, 3000 km s^{-1} is a velocity fully compatible with a wind: the WO component has a terminal velocity of 4500 km s^{-1}. A feature extending similarly to the blue (and actually very similar in shape to a mirror image of the RAEE in the second family of residual spectra) is visible half a period later as a BAEE (4595–4660 Å) as shown in Fig. 14. It is very tempting to associate these two features and to consider them as two different symptoms of the same phenomenon. Some kind of high velocity flow of matter approximately situated, for example, behind the O star with respect to the WO star (see Fig. 14) would present, provided it is emitting, redshifted EE at the conjunction with the WO in front ($\phi \sim 0.5$) and blueshifted EE when the O star is in front ($\phi \sim 0.0$). These BEE and REE features would be, as observed, in quadrature with respect to the orbital radial velocities.

It is necessary to remark here that both features (BAEE and RAEE) are not shifted towards the blue and the red with the same amplitude with respect to the centre of the blend at $\lambda = 4658$ Å (which is also the centre of the parabolic line at rest). The perception of the flow, when pointing towards the observer or when pointing away from him, may be asymmetrical (e.g. because of radiative transfer effects, occultations, …). An alternative explanation, preserving the symmetry, could be that the ionization of the matter that emits the EE differs from that of the WO wind, so that the EE would not necessarily correspond to a C IV emission. If we consider the flow to be geometrically symmetrical, the centre of symmetry of the BAEE and the RAEE is roughly around 4650 Å, which could suggest that the main contributor to both of these AEEs is indeed C III λλ4647–4650.

In massive binary systems, where both stars have strong

energetic winds, the interaction between these winds generates a shock region at their interface (e.g. Stevens, Blondin & Pollock 1992; Eichler & Usov 1993). Usually, one wind has stronger momentum than the other and a bow shock appears that is a curved surface with the concave side facing the star with the weaker wind. The collision of the two winds leads to an important increase of the density in the shock. The shocked material is also heated up to high temperatures especially near the binary axis where the two winds collide nearly head-on. As a first approximation, the shape of the interaction region can be described as a cone or very nearly so (i.e. a conoid) whose opening angle is set by the wind momentum ratio (Girard & Willson 1987). O5 stars in the sample of Lamers & Leitherer (1993) have mass-loss rates in the range $1.3–5 \times 10^{-6}\,\mathrm{M_\odot\,yr^{-1}}$ and terminal velocities of the order of $3000\,\mathrm{km\,s^{-1}}$. If we assume a mass-loss rate for the WO component in WR 30a of $1–5 \times 10^{-5}\,\mathrm{M_\odot\,yr^{-1}}$ and a terminal velocity of $4500\,\mathrm{km\,s^{-1}}$, we compute a momentum ratio

$$\mathcal{R} = \left(\frac{\dot{M}_{\mathrm{WO}} v_{\infty,\mathrm{WO}}}{\dot{M}_{\mathrm{O}} v_{\infty,\mathrm{O}}}\right)^{1/2} = 1.7 \rightarrow 7.6 \qquad (11)$$

which indicates that the wind of the WO star is expected to overcome the one of its O star companion and that the shock should be wrapped around the latter. The corresponding opening angle θ of the cone (angle between the axis and the surface of the cone) should be between, respectively, 70° and 30° (Girard & Willson 1987; Eichler & Usov 1993). These values admit that the winds have reached their terminal velocities before they collide, which might not be the case. Indeed, a crude calculation, admitting reasonable values for $\mathcal{R}$ and typical β-velocity laws for the winds, confirms that, in most cases, none of the winds reach their terminal velocity before the head-on shock; this is particularly true for the O star wind with some values as low as 50 per cent of v_∞.

A conoid of shocked material like the one resulting from a wind–wind collision could indeed provide a natural explanation for the high velocity flow responsible for the redshifted and the blueshifted AEE features. Even then, the matter might be unable to emit the relevant line. The shocked material is heated to very high temperatures and, under certain circumstances (e.g. Stevens et al. 1992), the hot plasma will only cool adiabatically. In these cases, we do not expect that the shocked material will emit significant amounts of visible light. On the contrary, there are cases where radiative cooling is possible. To discriminate between the two extreme cases, Stevens et al. (1992) introduced a χ criterion which, calculated for the case of WR 30a, rather suggests an adiabatic case. However, this χ criterion rests on several simplifying hypotheses. The actual case might be different. We will mention here the terminal velocities which might not be reached due to the small distance between both stars, but also, for example, due to the effect of the radiative braking of the WO wind by the O radiation field (Gayley, Owocki & Cranmer 1997; Gayley & Owocki 1999).

The binary has a rather short period. In this case, it is usually accepted that the Coriolis forces bend the shock cone. Such bending essentially manifests itself as a shift in phase with the maximum excursion in velocity that lags behind the conjunction. The expected phase lag can be estimated to be given by

$$\Delta\phi = (1/360°)\ \mathrm{arctg}\left(\frac{K_{\mathrm{O}} + K_{\mathrm{WO}}}{\alpha\, v_{\infty,\mathrm{WO}} \sin i}\right) \qquad (12)$$

which gives 0.02 considering α to be as low as 0.8 and $i = 25°$. The parameter α takes into account the fact that the WO wind at the level of the O component has not yet reached its terminal velocity. In the case of WR 30a, we observe a lag of about 0.05. The discrepancy by a factor of 2.5 could be because of the crudeness of our estimate.

For single WC/WO stars, similar to the one in WR 30a, that have been modelled in detail [WR 111, WC5 (see Hillier & Miller 1999); Br 10, WC4 (see Gräfener et al. 1998; Gräfener, private communication); Br 93, WO3 (see Crowther et al. 2000)], the region in the wind where the dominant species shift from C V to C IV is situated between 15 and $25\,\mathrm{R_\odot}$. From the value derived for the projected major axis ($20\,\mathrm{R_\odot}$), and from the absence of eclipse, we conclude that the O component essentially orbits outside the C V region. Since the atmosphere models suggest that the C IV λ4658 blend is mainly formed by recombination (Crowther, private communication), it is likely that the line of the WO component would be largely unaffected by the O companion. In such a context, the AEE would indeed correspond to an actual EE coming from elsewhere in the system. Again the shock region is a natural place for such an EE to originate.

The EEs near conjunction are rather wide. Hereafter, we will adopt a common central wavelength for the EEs of 4650 Å. This hypothesis has been made to preserve the understandability of the discussion by neglecting the possible asymmetry of the flow. The latter being a secondary effect, this hypothesis certainly does not imply, in our mind, a choice about the nature of the spectroscopic transition responsible for the features. The RAEE roughly extends from -600 to $+3300\,\mathrm{km\,s^{-1}}$ and the BAEE from -3500 to $+600\,\mathrm{km\,s^{-1}}$. In both cases, the velocity goes from more than $3000\,\mathrm{km\,s^{-1}}$ to zero and even to an opposite velocity of $600\,\mathrm{km\,s^{-1}}$. A fully natural way to explain such velocities would be to invoke a complex geometry as well as projection effects.

We are now going to perform a rough comparison between our observations and the general predictions of two models. Lührs (1997) introduced a model for WR 79 inspired by the hydrodynamical model of Stevens et al. (1992) but which is much more elementary and only geometrical: the emitting matter is assumed to flow at a constant stream velocity on the surface of a perfect cone of opening angle θ. This surface can be a little thick mantle of thickness $\Delta\theta$. The opening angle of the cone offers a diversity of projections of the stream velocity. Near conjunction, the two extreme velocities are $v_{\mathrm{str}} \sin(i - \theta)$ and $v_{\mathrm{str}} \sin(i + \theta)$, which corresponds to the intersection of the cone with the plane perpendicular to the orbit passing through the observer. If the opening angle is larger than i, part of the velocity stream is projected to the opposite sign. This could explain why the BAEE and the RAEE have a small range of velocities in common. At quadrature, the extreme velocities correspond to the intersection of the cone with a plane perpendicular to the sky: we have $+v_{\mathrm{str}} \sin\theta$ and $-v_{\mathrm{str}} \sin\theta$. At phases 0.80 and 0.30, the AEE is weak and distributed over the whole range of possible velocities.

To fix the ideas, we can adopt a constant velocity of $+v_{\mathrm{str}} = 4500\,\mathrm{km\,s^{-1}}$. To have a maximum extension up to $3450\,\mathrm{km\,s^{-1}}$, we need to have $|90° - i - \theta| = 40°$. To reach $600\,\mathrm{km\,s^{-1}}$ in the opposite direction, we need $|90° - i + \theta| = 98°$. This gives $\theta = 29°$ and $i = 21°$. The value for i is not in contradiction with our above mentioned independent estimate. The other solution ($\theta = 69°$ and $i = 61°$) yields an inclination that is not compatible with the orbital movement and would lead to too small masses. At quadrature, an opening angle $\theta = 29°$ would ensure a projected velocity of 48 per cent of v_{str} in each direction. This would spread the emission from 4615 to 4685 Å. One has the feeling that the actual spread is slightly wider. In the Lührs (1997) model, usually the EE presents two peaks near the extreme

velocities. This is clearly not the case here: the simplest way to account for the lack of such a double peaked structure within the framework of the Lührs model is to assume a thicker mantle, i.e. to increase $\Delta\theta$. An alternative possibility is to assume a strong turbulence within the shocked wind region. Still another alternative would be to introduce a gradient in the velocity along the conoid; this last possibility is one of the main features of the models of Stevens & Howarth (1999) we discuss below. It should be stated that the constraints derived above, on the inclination and on the opening angles, are only meaningful in the framework of the applicability of Lührs' model to WR 30a.

Recently, Stevens & Howarth (1999) presented a wind collision model to explain the variations of the He I λ10830 line in several colliding wind binaries. Essentially, the geometrical features are very similar to those in the model of Lührs but the emissivity of the matter is different. Schematically, most of the emissivity comes from the intersection between the conoid (tilted as a result of the Coriolis force) and the orbital plane. This forms a heading wake and a trailing wake. The latter has more emissivity because the shock with the WR wind is stronger for it. The velocity of the matter evolves along the surface of the conoid. This latter property allows a velocity dispersion without projection effects contrary to the model of Lührs. In their fig. 7 (bottom), Stevens & Howarth (1999) show the predicted He I λ10830 line-profile variations. The contribution of the wind–wind interface is particularly visible. Although their model is not directly applicable to the case of WR 30a, the broad similarity between the contribution of their wind–wind interface and the EE we presented in Fig. 13 is striking if a shift of about 0.45 in phase is applied to the phases of Stevens & Howarth. Indeed a shift of 0.5 is caused by the fact that they define their zero-point on the basis of the other conjunction while the remaining 0.05 can be explained by a lower Coriolis tilt for the case of WR 30a. Of course, their model stands for an inclination angle of $i = 90°$. The light emitted in the wakes being the major contributor, a factor of $\sin i$ is the only necessary first-order modification to their predictions. The model of Stevens & Howarth (1999) has the advantage of being able to explain the apparition of the narrow peaks around zero velocities at phase 0.934–1.0. It also explains the rapid blue shift of the blue edge of the REE at phase 0.6–0.7 (as also does the Lührs model). These latter characteristics are intimately linked to the rather large value of the opening angle which is around 45°. The correspondence between the emission of the wind–wind interface in the Stevens & Howarth (1999) model and in WR 30a is far from perfect. This is not surprising owing to the lack of direct applicability of the model hypotheses to the case of WR 30a (the model concerns He I λ10830). In general, the positions of the peaks are more or less good but the intensities are not. We finally remark that the ambiguity between the dispersion in true stream velocities and the projection effects does not authorize us to impose restrictions on the inclination of WR 30a without a detailed physical modelling. However, as in the case of Lührs' model, the one of Stevens & Howarth (1999) also suggests a rather wide opening angle of the conoid.

We compared our data with the generic models on the basis of the geometrical issues only. A detailed physical modelling is necessary to draw definitive conclusions; it is far beyond the scope of the present paper to derive such a model for the wind interactions in WR 30a. However, on the basis of both simple arguments and similarities demonstrated above between the line-profile variations of the C IV blend and the predictions of the current wind collision models, we can safely conclude that such a phenomenon is necessarily acting in the binary system WR 30a. Detailed modelling should ultimately allow to constrain the inclination of the system and therefore to derive accurate masses for both stars. Such an information is expected to be constraining for evolutionary models: a WO4 is a very evolved star in a stage for which mass information is particularly sparse whereas its companion is only weakly evolved. A model of the wind interaction should also lead to a measure of the exact momentum ratio of the two winds which could provide decisive information about mass-loss rates in massive stars.

From the observational point of view, true extra emissions at high velocities superimposed on the WR profiles, on the red side (after conjunction with the WR in front) and on the blue side (after the other conjunction) seem to be a generic characteristic of the WR + O colliding wind binary systems observed by Stevens & Howarth (1999). In the particular case of the He I λ10830 line, these extra emissions could be more persistent in phase than observed in the C IV line of WR 30a.

The archetype WR 79 is a well-known colliding wind system which motivated Lührs' model. It exhibits an extra emission in C III lines which is superimposed on flat topped profiles and oscillates in position. The latter is easy to follow over the whole cycle and the EE exhibits minor changes of its width over the whole cycle. This is clearly not the case for WR 30a.

The photometric variability of WR 30a is not straightforward to interpret. The star exhibits its lower luminosity at phase 0.05 (0.25 d after conjunction with the O in front), and its higher luminosity at phase 0.55. As suggested by the phase, the changes in the *V* band could at first sight be ascribed to the profile variability of the WO lines but the variations of the C IV λ4658 equivalent width are bimodal over the period of the system whereas the photometric variability is unimodal. An inhomogeneity in the temperature of the O star surface because of the WO and the wind–wind interaction is another possibility. The fact that the spectral type is not phase dependent could be explained by temperature inhomogeneities remaining much lower than the difference with the neighbouring spectral types. Another possibility of asymmetry could come from the wind collision itself. Indeed, Gayley et al. (1997) and Gayley & Owocki (1999) suggested that the O star in such a system could perform a radiative braking on the WR wind approaching it. In such a case, the radiation of the O starlight that impinges on the braking zone must be reflected. Such a phenomenon could in principle enhance the emission of the system when the O star is in front, which is exactly the opposite of what is observed. Another possibility would be that the WO photosphere would be perturbed by the presence of the shock and the wind interaction. WO stars can have very extended atmospheres and a wind collision arising in the WR wind could hollow out part of the WO atmosphere. Such an effect should be modelled along with the wind interaction. Finally, for some inclination angles, it is possible that the O star occults part of the wind of the WO component. The absence of atmospheric eclipse when the WO is in front is certainly a restriction on this possibility. It is interesting to note that the binary star SMC AB8 (WO4 + O7) exhibits photometric variations of amplitude 0.025 mag very similar to those of WR 30a (Moffat, Breysacher & Seggewiss 1985).

At phase 0.7, the O star seems to develop narrow emissions. This essentially concerns N III $\lambda\lambda$4634–4641; He II λ4686 is also influenced and other lines may follow the same trend. Our spectra do not allow to perform a detailed analysis of this emission and of its possible evolution with phase: we are thus unable to locate it precisely in the system. However, the

morphology of the lines suggests a relation with the O star. Phase 0.7 corresponds to a moment when the O star comes towards the observer and where the apex of the conoid and the head-on collision point are particularly visible without occultation. It is tempting to associate these narrow emissions with the shock or with the atmosphere of the O star just below it. If true, a full interpretation of this phenomenon could most probably provide information on this region and even perhaps on secondary mechanisms such as the radiative braking (Gayley et al. 1997; Gayley & Owocki 1999).

The present Roche lobe critical radius associated to the O star is $R_{\rm RL} \sin i = 10.8\,{\rm R}_\odot$. For inclinations lower than 33°, the star is certainly not filling its lobe, and overflow through the inner Lagrangian point could not contribute to explain the narrow emissions.

6 CONCLUSIONS

We presented a detailed, extensive investigation of the photometric and spectroscopic behaviour of WR 30a. As a conclusion, WR 30a is definitely a binary system with a period around 4.6 d. We propose the value $P = 4.619$ d ($\sigma = 0.002$ d). The identification of the components, WO4 + O5((f)), indicates a massive evolved binary system; the O5 component is a main-sequence or, more likely, a giant star. Our spectroscopic data outline the motion of the O star, giving a circular orbit with $K_{\rm O} = 29.9\,(\sigma = 2.1)\,{\rm km\,s^{-1}}$ and a mass function of $0.013\ (\sigma = 0.003)\,{\rm M}_\odot$. The situation is not so easy for the WO component because the WO line we studied exhibits strong line-profile variations that are phase-locked with the orbital period. In any case, we propose a $K_{\rm WO} = 189\,{\rm km\,s^{-1}}$ that needs further confirmation. If correct, this value implies a mass ratio $M_{\rm WO}/M_{\rm O} = 0.16$ and $M_{\rm O} \sin^3 i = 4.34\,{\rm M}_\odot$, $M_{\rm WO} \sin^3 i = 0.69\,{\rm M}_\odot$ and $a \sin i = 20\,{\rm R}_\odot$. The photometry exhibits sinusoidal variations of 0.024 mag (peak-to-peak), the star being fainter a little after the conjunction with the O star in front. The phase-locked profile variations of the C IV λ4658 WO blend are strongly reminiscent of what is expected from a wind–wind collision phenomenon in the system. A detailed modelling of the phenomenon should allow to put further constraints on the parameters such as the inclination of the system.

In the near future, the study of WR 30a will certainly provide some clues on massive star evolution, but more observations are necessary. The next radial velocity curve for the O star should be ascertained as being free of biases coming from possible line-profile variations. Indeed, a very accurate radial velocity curve should allow to derive the exact eccentricity which will never be derived from the WO component. Also, observations of a whole variety of lines of this WO component, implying to go away partially from the visible domain, should allow to disentangle fully the orbital motion and the wind–wind interaction and, consequently, to reach a better understanding of the detailed physical processes leading to the wind interaction.

ACKNOWLEDGMENTS

The authors are greatly indebted to G. Gräfener and to P. A. Crowther for communicating details about their respective models. Comments on the paper by P. A. Crowther have led to significant improvements. The authors are also grateful to H. G. Grothues who greatly helped them in negotiating the access to the Bochum telescope, as well as to the FNRS that provided funds to operate this telescope during one month. The authors thank the FNRS for multiple supports in general. This research is also backed up by contract P4/05 'Pôle d'Attraction Interuniversitaire' (SSTC-Belgium) and by the PRODEX XMM-OM and INTEGRAL Projects which are also gratefully acknowledged. The Simbad data base has been recurrently consulted. This work was based on observations acquired at the European Southern Observatory and at the Bochum telescope, La Silla, Chile, as well as at the Cerro Tololo Interamerican Observatory, Chile.

REFERENCES

Cami J., Sonnentrucker P., Ehrenfreund P., Foing B. H., 1997, A&A, 326, 822
Conti P. S., 1973a, ApJ, 179, 161
Conti P. S., 1973b, ApJ, 179, 181
Conti P. S., Massey P., 1989, ApJ, 337, 251
Conti P. S., Leep E. M., Lorre J. J., 1977, ApJ, 214, 759
Crowther P. A., De Marco O., Barlow M. J., 1998, MNRAS, 296, 367
Crowther P. A. et al., 2000, ApJ, 538, L51
Eichler D., Usov V., 1993, ApJ, 402, 271
Foster G., 1995, AJ, 109, 1889
Gayley K. G., Owocki S. P., 1999, in van der Hucht K. A., Koenigsberger G., Eenens P. R. J., eds, Proc. IAU Symp. 193, WR Phenomena in Massive Stars and Starburst Galaxies. Astron. Soc. Pac., San Francisco, p. 168
Gayley K. G., Owocki S. P., Cranmer S. R., 1997, ApJ, 475, 786
Girard T., Willson L. A., 1987, A&A, 183, 247
Gosset E., Royer P., Rauw G., Manfroid J., Vreux J. M., 1999, in van der Hucht K. A., Koenigsberger G., Eenens P. R. J., eds, Proc. IAU Symp. 193, WR Phenomena in Massive Stars and Starburst Galaxies. Astron. Soc. Pac., San Francisco, p. 354
Gräfener G., Hamann W. R., Hillier D. J., Koesterke L., 1998, A&A, 329, 190
Heck A., Manfroid J., Mersch G., 1985, A&AS, 59, 63
Herbig G. H., 1995, ARA&A, 33, 19
Hillier D. J., Miller D. L., 1999, ApJ, 519, 354
Howarth I. D., Prinja R. K., 1989, ApJS, 69, 527
Kingsburgh R. L., Barlow M. J., Storey P. J., 1995, A&A, 295, 75
Lamers H. J. G. L. M., Leitherer C., 1993, ApJ, 412, 771
Lépine S., Moffat A. F. J., Henriksen R. N., 1996, ApJ, 466, 392
Lührs S., 1997, PASP, 109, 504
Lundström I., Stenholm B., 1984a, A&AS, 58, 163
Lundström I., Stenholm B., 1984b, A&A, 138, 311
Mathys G., 1988, A&AS, 76, 427
McConnell D. J., Sanduleak N., 1970, PASP, 82, 80
Moffat A. F. J., Seggewiss W., 1984, A&AS, 58, 117
Moffat A. F. J., Breysacher J., Seggewiss W., 1985, ApJ, 292, 511
Moffat A. F. J., Niemela V., Marraco H. G., 1990, ApJ, 348, 232
Morrell N. I., Walborn N. R., Fitzpatrick E. L., 1991, PASP, 103, 341 (Addendum: 1049)
Niemela V., 1995, in van der Hucht K. A., Williams P. M., eds, Proc. IAU Symp. 163, Wolf–Rayet stars: binaries, colliding winds, evolution. Kluwer, Dordrecht, p. 223
Norci L., Polcaro V. F., Rossi C., Viotti R., 1998, Irish Astron. J., 25, 1, 43
Polcaro V. F., Norci L., Rossi C., Viotti R., 1999, in van der Hucht K. A., Koenigsberger G., Eenens P. R. J., eds, Proc. IAU Symp. 193, Wolf–Rayet Phenomena in Massive Stars and Starburst Galaxies. Astron. Soc. Pac., San Francisco, p. 88
Renson P., 1978, A&A, 63, 125
Scargle J. D., 1982, ApJ, 263, 835
Scholz M., 1972, A&AS, 7, 469
Smith L. F., 1968, MNRAS, 140, 409
Smith L. F., Shara M. M., Moffat A. F. J., 1990a, ApJ, 348, 471
Smith L. F., Shara M. M., Moffat A. F. J., 1990b, ApJ, 358, 229
Stenholm B., 1975, A&A, 39, 307
Stetson P. B., 1987, PASP, 99, 191
Stevens I. R., Howarth I. D., 1999, MNRAS, 302, 549

Stevens I. R., Blondin J. M., Pollock A. M. T., 1992, ApJ, 386, 265
Torres A. V., Massey P., 1987, ApJS, 65, 459
Turatto M., Tighe R., Castillo R., 1997, ESO Technical Report NoE15-TRE-ESO-22201-0001
Underhill A. B., 1995, ApJS, 100, 433
van der Hucht K. A., 2001, New Astron. Rev., 45, 135
van der Hucht K. A., Conti P. S., Lundström I., Stenholm B., 1981, Space Sci. Rev., 28, 227
Vreux J. M., Gosset E., Bohannan B., Conti P. S., 1992, A&A, 256, 148
Walborn N. R., Fitzpatrick E. L., 1990, PASP, 102, 379
Wramdemark S., 1976, A&AS, 23, 231

APPENDIX A: THE CORRECT POWER SPECTRUM AND ITS GENERALIZATION

HMM (1985) proposed a sound mathematical expression for the estimate of the power spectrum of an unevenly sampled time series. Unfortunately, the original paper suffered from mistakes in some equations. We recall the method here while giving the corrected expressions.

The Fourier method is equivalent, at each frequency ν, to a least-squares fitting of a sine curve to the observed data. The time series is made of N_0 data points $x_i = x(t_i)$ ordered in the vector $\boldsymbol{X}$, and the linear form of the function is

$$g(t_i) = \mu + a\cos 2\pi\nu t_i + b\sin 2\pi\nu t_i. \tag{A1}$$

We can define the N_0 by 2 matrix $\boldsymbol{A}(\nu)$ whose elements are, for i between 1 and N_0,

$$A_{i1}(\nu) = \cos 2\pi\nu t_i - \bar{C}(\nu) \tag{A2}$$

$$A_{i2}(\nu) = \sin 2\pi\nu t_i - \bar{S}(\nu) \tag{A3}$$

where

$$\bar{C}(\nu) = N_0^{-1}\sum_{i=1}^{N_0}\cos 2\pi\nu t_i \tag{A4}$$

$$\bar{S}(\nu) = N_0^{-1}\sum_{i=1}^{N_0}\sin 2\pi\nu t_i \tag{A5}$$

The residual sum of squares of the data around their estimated mean is given by the quadratic form

$$RSS_0 = \tilde{\boldsymbol{X}}\boldsymbol{F}_0\boldsymbol{X} \tag{A6}$$

where

$$\boldsymbol{F}_0 = \boldsymbol{I} - N_0^{-1}\boldsymbol{e}\tilde{\boldsymbol{e}} \tag{A7}$$

and where $\boldsymbol{I}$ is the identity matrix and $\boldsymbol{e}$ a vertical vector of length N_0 with 1 everywhere. Under the hypothesis that the time series is generated by a Gaussian (or assimilable) white-noise process of variance σ^2, $\sigma^{-2}RSS_0$ is distributed like a chi-square with $N_0 - 1$ degrees of freedom. The residual sum of squares of the data around the fitted sine curve is given by the quadratic form

$$RSS_1(\nu) = \tilde{\boldsymbol{X}}\boldsymbol{F}_1\boldsymbol{X} \tag{A8}$$

where

$$\boldsymbol{F}_1 = \boldsymbol{I} - N_0^{-1}\boldsymbol{e}\tilde{\boldsymbol{e}} - \boldsymbol{A}(\nu)[\tilde{\boldsymbol{A}}(\nu)\boldsymbol{A}(\nu)]^{-1}\tilde{\boldsymbol{A}}(\nu). \tag{A9}$$

Similarly, $\sigma^{-2}RSS_1$ is distributed like a chi-square with $N_0 - 3$ degrees of freedom. The sound expression for the power spectrum is proportional to

$$SP(\nu) = RSS_0 - RSS_1(\nu) = \tilde{\boldsymbol{X}}(\boldsymbol{F}_0 - \boldsymbol{F}_1)\boldsymbol{X} \tag{A10}$$

and $\sigma^{-2}SP(\nu)$ is distributed according to a chi-square with two degrees of freedom. The correct statistic is given by the ratio of the two independent chi-square variates

$$\theta_{\rm F}(\nu) = SP(\nu)/RSS_1(\nu) \tag{A11}$$

and

$$\frac{N_0 - 3}{2}\theta_{\rm F} \tag{A12}$$

is thus distributed like a Snedecor F-distribution with 2 and $N_0 - 3$ degrees of freedom. We can also define the amplitude spectrum which has the nature of the square root of the power spectrum normalized so that it directly gives the semi-amplitude of the sine curve.

The generalization towards the simultaneous fit of M frequencies can be similarly computed by defining the $\boldsymbol{A}(\nu^{(1)}, \nu^{(2)}, \ldots, \nu^{(M)})$ matrix. We obtain

$$A_{i1}(\nu^{(1)}) = \cos 2\pi\nu^{(1)}t_i - \bar{C}(\nu^{(1)}) \tag{A13}$$

$$A_{i2}(\nu^{(1)}) = \sin 2\pi\nu^{(1)}t_i - \bar{S}(\nu^{(1)}) \tag{A14}$$

$$A_{i3}(\nu^{(2)}) = \cos 2\pi\nu^{(2)}t_i - \bar{C}(\nu^{(2)}) \tag{A15}$$

$$A_{i4}(\nu^{(2)}) = \sin 2\pi\nu^{(2)}t_i - \bar{S}(\nu^{(2)}) \tag{A16}$$

$\ddots$

$\ddots$

$$A_{i(2M-1)}(\nu^{(M)}) = \cos 2\pi\nu^{(M)}t_i - \bar{C}(\nu^{(M)}) \tag{A17}$$

$$A_{i(2M)}(\nu^{(M)}) = \sin 2\pi\nu^{(M)}t_i - \bar{S}(\nu^{(M)}). \tag{A18}$$

The generalized

$$\frac{N_0 - 2M - 1}{2M}\theta_{\rm F} \tag{A19}$$

is similarly distributed with $2M$ and $N_0 - 2M - 1$ degrees of freedom provided M is not too large compared to $\frac{N_0-1}{2}$.

This paper has been typeset from a TEX/LATEX file prepared by the author.